Publication Year	2023
Acceptance in OA	2025-02-07T10:13:41Z
Title	Diffuse X-Ray Emission in the Cygnus OB2 Association
Authors	Albacete-Colombo, J. F., Drake, J. J., FLACCOMIO, Ettore, Wright, N. J., Kashyap, V., GUARCELLO, Mario Giuseppe, Briggs, K., Drew, J. E., Fenech, D. M., MICELA, Giuseppina, McCollough, M., Prinja, R. K., Schneider, N., SCIORTINO, Salvatore, Vink, J. S.
Publisher's version (DOI)	10.3847/1538-4365/acdd65
Handle	http://hdl.handle.net/20.500.12386/35844
Journal	THE ASTROPHYSICAL JOURNAL SUPPLEMENT SERIES
Volume	269

The Astrophysical Journal Supplement Series, 269:14 (23pp), 2023 November https://doi.org/10.3847/1538-4365/acdd65

Diffuse X-Ray Emission in the Cygnus OB2 Association

J. F. Albacete-Colombo[1], J. J. Drake[2], E. Flaccomio[3], N. J. Wright[4], V. Kashyap[2], M. G. Guarcello[3], K. Briggs[5], J. E. Drew[6], D. M. Fenech[7], G. Micela[3], M. McCollough[2], R. K. Prinja[7], N. Schneider[8], S. Sciortino[3], and J. S. Vink[9]

[1] Universidad de Río Negro, Sede Atlántica, Viedma CP8500, Argentina; albacete.facundo@conicet.gov.ar
[2] Smithsonian Astrophysical Observatory, 60 Garden St., Cambridge, MA 02138, USA
[3] INAF-Osservatorio Astronomico di Palermo, Piazza del Parlamento 1, I-90134 Palermo, Italy
[4] Astrophysics Group, Keele University, Keele, Staffordshire ST5 5BG, UK
[5] Hamburger Sternwarte, University of Hamburg, Gojenbergsweg 112, D-21029, Hamburg, Germany
[6] School of Physics, Astronomy & Mathematics, University of Hertfordshire, College Lane, Hatfield, Hertfordshire AL10 9AB, UK
[7] Department of Physics and Astronomy, University College London, Gower Street, London WC1E 6BT, UK
[8] I. Physik. Institut, University of Cologne, D-50937 Cologne, Germany
[9] Armagh Observatory and Planetarium, College Hill, Armagh BT61 9DG, UK

Received 2018 March 28; revised 2018 May 30; accepted 2018 May 31; published 2023 October 25

Abstract

We present a large-scale study of diffuse X-ray emission in the nearby massive stellar association Cygnus OB2 as part of the Chandra Cygnus OB2 Legacy Program. We used 40 Chandra X-ray ACIS-I observations covering ∼1.0 deg^2. After removing 7924 point sources detected in our survey and applying adaptive smoothing to the background-corrected X-ray emission, the adaptive smoothing reveals large-scale diffuse X-ray emission. Diffuse emission was detected in the subbands soft (0.5−1.2 keV) and medium (1.2−2.5 keV) and marginally in the hard (2.5−7.0 keV) band. From X-ray spectral analysis of stacked spectra we compute a total (0.5–7.0 keV) diffuse X-ray luminosity of $L_X^{\rm diff} \approx 4.2 \times 10^{34}$ erg s^{-1}, characterized by plasma temperature components at $kT \approx 0.11$, 0.40, and 1.18 keV, respectively. The H I absorption column density corresponding to these temperatures has a distribution consistent with $N_{\rm H} = (0.43, 0.80, 1.39) \times 10^{22}$ cm^{-2}. The extended medium-band energy emission likely arises from O-type stellar winds thermalized by wind−wind collisions in the most populated regions of the association, while the soft-band emission probably arises from less energetic termination shocks against the surrounding interstellar medium. Supersoft and soft diffuse emission appears more widely dispersed and intense than the medium-band emission. The diffuse X-ray emission is generally spatially coincident with low-extinction regions that we attribute to the ubiquitous influence of powerful stellar winds from massive stars and their interaction with the local interstellar medium. Diffuse X-ray emission is volume filling, rather than edge brightened, oppositely to other star-forming regions. We reveal the first observational evidence of X-ray halos around some evolved massive stars.

Unified Astronomy Thesaurus concepts: X-ray stars (1823); Massive stars (732); Stellar winds (1636)

1. Introduction

Since the early X-ray observations by Einstein and later ROSAT, and up to the last decade, the study of diffuse X-ray emission associated with stellar clusters and star-forming regions (SFRs) has presented considerable challenges. While in supernova remnants or large-scale massive structures, such as galaxy clusters, detections can be quite clear, confirmation of diffuse X-ray emission from Galactic SFRs has often remained elusive. Several attempts were made to detect diffuse X-rays from young massive SFRs with ROSAT (e.g., Strickland & Stevens 1998). However, the lack of adequate sensitivity and spatial resolution rendered it difficult to distinguish between genuine diffuse emission and X-ray emission from unresolved stars. Limited by the available instrumentation, this subfield of astrophysics remained without major progress for more than 20 yr. This ended in 1999 with the launch of the Chandra X-ray Observatory, which combines high sensitivity in the 0.5–8 keV energy range with spectacular spatial resolution (≈0.″5 on axis). This combination greatly improved the capacity to detect faint X-ray sources and disentangle point-source and true diffuse emission contributions in nearby Galactic SFRs. The first genuine discovery of diffuse X-ray emission in a massive star-forming region came from the Rosette and Omega Nebulae (Townsley et al. 2003; Muno et al. 2006). Subsequently, XMM-Newton observations of the Orion Nebula revealed it to be filled by soft X-ray-emitting (2 MK) plasma (Güdel et al. 2008). More recently, in the context of the "Chandra Carina Complex Project" (CCCP), Townsley et al. (2011a) have published a milestone work for study of X-ray diffuse emission in Carina.

From a theoretical point of view, diffuse X-ray emission is expected to occur in some young stellar associations and SFRs owing to supersonic stellar winds from massive stars that can produce dissipative shock waves in the local interstellar medium (ISM), modifying astrophysical conditions of the molecular cloud material in the region. These shocks have been interpreted as evidence of nonradiative heating processes (Polcaro et al. 1991) that can give rise to a number of interesting, though poorly explored, high-energy phenomena. However, the processes responsible for the production of X-ray diffuse emission are still not well understood, especially where both thermal and nonthermal (NT) processes may be present. A usual key indicator of thermal diffuse X-ray emission is the presence of spectral lines (Smith et al. 2001), although NT interactions can also produce intense and relatively soft X-ray emission lines ($<$2 keV) via the charge X-ray exchange (CXE) mechanism. Otherwise, a featureless spectrum without lines can originate from either thermal processes (e.g., hot bremsstrahlung) or NT electrons via synchrotron emission or inverse Compton (IC) scattering processes.

The first detailed theoretical study was performed in a seminal paper by Weaver et al. (1977). Further development of models for X-ray emission from wind-blown bubbles was carried out by Cantó et al. (2000) and Stevens & Hartwell (2003): they interpreted diffuse X-ray emission associated with massive clusters in terms of a collective cluster wind model (CWM). Winds from individual massive stars with mass-loss rates of $\sim 10^{-6}\ M_{\odot}\ \mathrm{yr}^{-1}$ and terminal speeds of 1600–2500 km s^{-1} collide, thermalize, and expand supersonically into the local ISM. This interaction acts as a precursor of an "interstellar bubble" that expands to a few tenths of a parsec around stars more massive than $\sim 8\,M_{\odot}$. Approximate estimates for a typical single O and/or early B star luminosity and wind kinetic energy are $L_{\mathrm{bol}} \sim 10^{38}$–$10^{39}$ erg s^{-1} and $L_{\mathrm{w}} \sim 10^{36}$–$10^{37}$ erg s^{-1}, respectively. The adopted typical efficiency of wind momentum to radiative conversion η is 10^{-4} for interstellar shocks (Güdel et al. 2008), resulting in an X-ray diffuse emission luminosity $L_{\mathrm{X}}^{\mathrm{diffuse}} \sim 10^{33} - 10^{34}$ erg s^{-1}.

However, models of such wind-blown bubbles predict much larger sizes than those reported by Bruhweiler et al. (2010) for the example of the Rosette Nebula. The discrepancy implies that the shocks involved should occur in the radiative (energy-loss) regime. Otherwise, the high wind speeds should produce strong $\sim$keV X-ray diffuse emission within regions with scales of a few parsecs. At the same time, evidence for very large "superbubbles" enclosing entire OB associations and shaped by multiple supernovae has been presented. The particular case of the Cygnus superbubble, on a scale well in excess of 100 pc (Cash et al. 1980), is relevant here. But Uyaniker et al. (2001) have argued that the extensive X-ray emission is better viewed as a superposition of a succession of separate regions at different distances. Accordingly, in Cygnus an investigation of improving high-energy data can make a valuable contribution to clarifying our understanding, and we can access spatial scales of up to tenths of a parsec.

In this work, we identify truly diffuse X-ray emission in the Cygnus OB2 association, one of the most massive groups of young stars known in the Galaxy. Assessments of its stellar complement have found that Cygnus OB2 contains well over 100 OB stars (e.g., Schulte 1956; Massey & Thompson 1991; Comerón et al. 2002; Hanson 2003; Wright et al. 2015b) and tens of thousands of lower-mass, pre-main-sequence (PMS) stars (e.g., Albacete Colombo et al. 2007; Drew et al. 2008; Vink et al. 2008; Wright & Drake 2009). Cygnus OB2 lies at the center of the Cygnus X giant molecular cloud and star-forming complex (Schneider et al. 2006; Reipurth & Schneider 2008) and is a source of feedback for the region (Wright et al. 2012; Guarcello et al. 2023a). Its size and proximity make Cygnus OB2 an ideal environment to search for diffuse emission resulting from feedback into the environment from massive stars.

This study forms a part of the science exploitation of the Chandra Cygnus OB2 Legacy Survey. This 1.1 Ms survey comprises a mosaic of Chandra ACIS-I pointings covering the central square degree of the association, which contains the majority of the massive young stellar association. The observations and the source catalog are described in Wright et al. (2023a). Guarcello et al. (2023b) have matched X-ray sources with available optical and infrared (IR) photometric catalogs, while Kashyap et al. (2023) have applied statistical methods to separate out $\sim$6000 sources identified as association members from an additional $\sim$2000 sources assessed as foreground and background interlopers. Flaccomio et. al. (2023) characterize the X-ray spectral properties of these populations and discuss the results in the context of different emission models. This thorough assessment of the point-source content, combined with the deep and wide nature of the Chandra survey itself, provides a valuable data set for a thorough exploration of X-rays from diffuse gas in the region.

In this article we focus on the analysis, detection and morphological description of diffuse X-ray emission in Cygnus OB2. We discuss its origin and derive approximate astrophysical properties of the diffuse X-ray structures at large and small scales.

2. X-Ray Observations and Diffuse Emission Analysis

The study of the diffuse X-ray emission is of interest for assessing the total X-ray output of a region like Cygnus OB2 and will be important for understanding the X-ray emission from much more distant, unresolved stellar clusters. The expected diffuse X-ray emission from Cyg OB2 will be spread over a large angular sky area ($\sim$1 deg^2) and will have a correspondingly low surface brightness. An interesting rough comparison is the expected diffuse signal compared with the combined signal from detected point sources. We can estimate the X-ray luminosity of the detected Cygnus OB2 stellar population by assuming that (i) we detect all members with mass $>1\,M_{\odot}$ (Wright et al. 2023b), (ii) the initial mass function of Cygnus OB2 is similar to that of the Orion Nebula Cluster (ONC), and (iii) Cygnus OB2 stars have the same X-ray activity as derived for ONC stars by Preibisch et al. (2005). Adopting the "lightly absorbed optical sample" as representative of the low-mass ONC population, we estimate that the Cygnus OB2 population of stars with mass between 1.0 and 10 $M_{\odot}$ is $\sim$10 times larger than the ONC one. We can then scale the total luminosity of the ONC sample by this factor, obtaining $L_{\mathrm{X}}^{\mathrm{LMS\ total}} \sim 2 \times 10^{34}$ erg s^{-1} for the whole association, which is comparable to what we expect for the diffuse emission. To deal successfully with the difficult task of extracting the diffuse emission signal, we made use of the specific data analysis software ACIS-Extract (AE; Broos et al. 2012), which is able to remove the point-source X-ray emission via the construction of "swiss-cheese" ACIS-I images with holes at the positions of detected point sources. It computes the local point-spread function (PSF) at each source position and masks its local contribution to the observation (see Section 2). However, the removal of all detected point sources does not of course guarantee that the remaining X-ray emission will be truly diffuse, since the summed contribution of undetected faint sources could masquerade as diffuse X-ray emission. To assess how big this problem is, we adopt the completeness limit of the survey in the central 0.5 deg^2 as computed by Wright et al. (2023b). Assuming that the distribution of X-ray luminosities at a given mass is the same as in the ONC, as sampled by the Chandra Orion Ultradeep Project (COUP) "lightly absorbed optical sample," and that the population is 10 times as large (see above), we estimate that the X-ray luminosity of the undetected population of sources is $\sim 4.5 \times 10^{33}$ erg s^{-1}.

2.1. Data Reduction and Processing

We made use of the set of 37 X-ray pointings of the Chandra ACIS-I camera that were acquired in the context of the Chandra Cygnus OB2 Legacy Program. An additional set of three existing observations were included within the survey area, which had previously been used to study the Cyg OB2 association (Butt et al. 2006; Albacete Colombo et al. 2007; Wright & Drake 2009). The total of 40 pointings were acquired in the VFAINT (5 × 5 pixel island) mode, which is an optimal choice for identifying and removing events that originate from the endpoints of particle event tracks and that cannot be removed using a standard grade analysis based on 3 × 3 islands.[10] This observational setup is crucial to disentangling true X-ray diffuse emission photons from instrumental and background effects. The survey was performed over a central 0.5 deg^2 of the Cygnus OB2 association with an effective exposure of 120 ks and an outer 0.35 deg^2 area with an exposure of 60 ks. The description of the survey design and observations, data reduction, and source detection has been presented extensively in Wright et al. (2023a).

All 40 ObsIDs were uniformly reprocessed using version 4.8 of the CIAO software (Fruscione 2014), combined with CALDB 4.7.1 calibration database files. In order to get consistency in the calibration procedure, we reran the Level 1 to Level 2 processing of event files using the CIAO CHANDRA_REPRO meta task. The CHECK_VF_PHA=YES option was set to flag bad events and then filter them. The new Level 2 event file was produced by filtering events to status == b0. The initial set of observations were processed with older *gain* files and were updated during the ACIS_PROCESS_EVENT to the lastest available file version. Similar treatment was applied to the background event files (see Section 2.1 for details). Since the available "stowed" background files (from which the energetic particle event background can be estimated) were made using only quiescent background periods, background flares needed to be excluded from our observations in exactly the same way for consistency. We extracted light curves with the same time bin size as was performed for the background files (bin = 259.28 s), and we made use of the DEFLARE CIAO 4.8 Python routine.[11] We time-filtered all of the observations. The time reduction was found to be necessary, and in the worst case this amounted to less than 4% of the total exposure of an observation. In order to avoid intense instrumental emission lines (see Section 2.2), we filtered the whole set of observations to exclude all events outside of the 0.5–7.0 keV energy range.

The reprocessed event files and this set of observations are essentially the starting point of our analysis. We computed monochromatic exposure maps for all 40 X-ray observations using the AE_MAKE_EMAP AE task for representative photon energies of 0.7, 1.7, and 3.5 keV. In Figure 1, we show the mosaic of exposures at 1.7 keV of all the observations used in the Cyg OB2 survey. We use each of these sets of images to normalize the count images in different energy bands of 0.5–1.2 keV, 1.2–2.5 keV, and 2.5–7.0 keV, respectively, to produce X-ray flux images uncorrected for interstellar absorption. However, as the diffuse X-ray emission is faint, the confirmation of its existence depends on careful analysis of the background (Section 2.2), as well as a thorough assessment of the contribution from X-ray point sources (Section 2.3).

2.2. Background Analysis

Analysis of faint extended X-ray diffuse emission is an inherently difficult task, as the emission is spread over the detector and is affected by nonlocal background such as solar and radiation belt energetic particle events and X-ray events from interloping sources such as active galactic nuclei (AGNs). As noted above, the instrumental and energetic particle background was assessed using a set of ACIS stowed observation files.[12] Since the ACIS instrumental background is known to be time varying, the proper scaling of these images to a given observation cannot be estimated from relative exposure times alone (see, e.g., details in Section 4.1.3 of Hickox & Markevitch 2006). Thus, background images were also scaled to match the spectra of each of the 40 observations in the 7–12 keV range, where the stellar emission has no significant signal (see Figure 2).

Finally, we constructed new stowed exposure maps for the next step of the analysis, which uses mask stowed event files and new stowed exposure maps for use at each source position.

2.3. Masking X-Ray Point Sources

Here we give details of the procedure implemented to reduce the impact of X-ray point sources on the event and calibration (stowed) data files. We used the specific task AE_MASK_STOWED_DATA from the AE code that masked event files, exposure maps, and both stowed events and stowed exposure files. We thus subtracted events from a total of 7924 X-ray point sources listed in our catalog (Wright et al. 2023a) covering all 40 of the ACIS-I observations.

The first step in the point-source subtraction is to build intensity models for sources, as well as for readout streaks, and draw masks around them to compute an image that models the signal from all these features. We use the task AE_BETTER_MASKING from AE to adaptively compute source emission at the 99% enclosed energy aperture threshold. Such a mask fraction is more than adequate for faint sources with only a handful of counts, since the probability of losing genuine source events in the PSF wings is low. In cases where the X-ray source was intense, the source wings were inspected close to the masked event data to see whether there were remaining wings from scattering photons that are bright enough to locally contaminate our diffuse emission analysis. In such cases, we arbitrarily increased the mask size by multiplying by up to a factor 1.5 the 99% PSF limit (Townsley et al. 2011a). Under this condition, the AE recipes assure that source event photons in the wings of the PSF, or photons scattered out of the PSF, should fall below the local background level of the observation (Broos et al. 2012). In the left panel of Figure 3, we show the resulting source + readout streak emission models. Otherwise, the right panel of Figure 3 shows the residual map of the cropped sources, which consist of the difference between the observed source count image and the source + streak intensity models (left panel). Hereafter we refer to these residual images as "wings" files. Note that the wings image peaks at log(Source wings) ≈ −1.45. This means that the maximum "wings" contribution to the observed emission image is only about 3.5%

---

[10] See further details in http://cxc.harvard.edu/Acis/Cal_prods/vfbkgrnd/.

[11] http://cxc.harvard.edu/ciao/ahelp/deflare.html

[12] http://cxc.cfa.harvard.edu/contrib/maxim/acisbg/data/

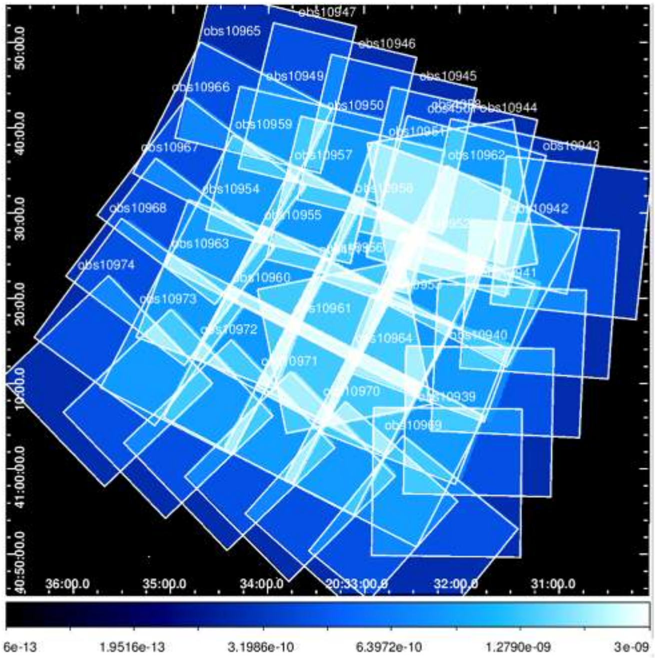

Figure 1. The exposure map for the Cygnus OB2 Chandra Legacy Survey and complementary observations for the study of diffuse X-ray emission. The bottom color bar shows the flux-to-color normalization factor in erg cm^{-2} s^{-1}.

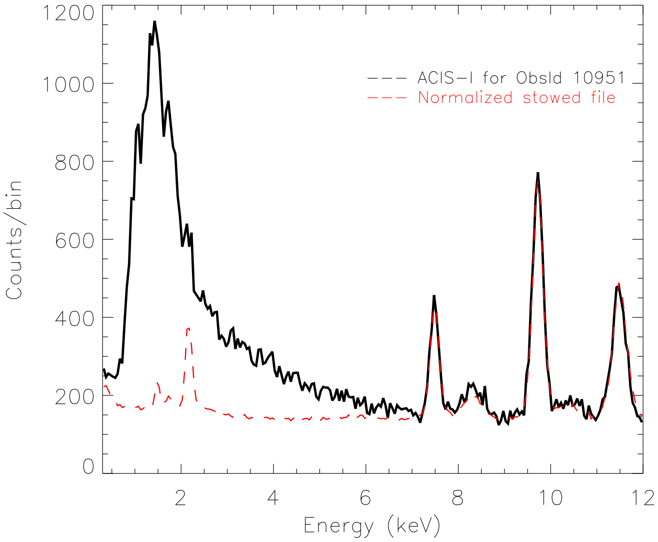

Figure 2. Pulse height distribution of events for ObsID 10951 (black solid line), together with the stowed background normalized to match based on fluxes at energies of 7.47, 9.8, and 11 keV, where the sky has no emission (red dashed line). The weaker ~2.1 keV emission line is also instrumental but was not used to match stowed observation events, and so it could be present in some diffuse X-ray spectra.

or less. Both maps shown correspond to ObsID 10951, which hereafter will be used to illustrate the analysis that was applied to the rest of the observations.

3. Adaptive Smoothing Strategy

One of the most critical issues in the study of X-ray diffuse emission is the choice of smoothing strategy. For this purpose, we made use of the TARA_SMOOTH tasks.[13] We used the top-hat adaptive kernel smoothing. All maps were computed in a 512×512 array. Larger 1024×1024 maps did not produce better results and were also computationally very demanding. Two main parameters that play a major role in smoothing are (i) the significance, which is a scalar or vector number specifying the desired signal-to-noise ratio (S/N) of the smoothed flux image, and (ii) the smoothing radii that could be imposed to achieve the same spatial smoothing scales in different energy bands. The radii of smoothing are limited to a maximum of 71 pixels, and the imposed S/N condition is only applied if smoothing radii remain below this limit. The smoothing procedure was initially run for the full 0.5–7.0 keV band. After several runs at S/Ns of 9, 12, 16, and 25, we found that S/N ~ 16 is the best compromise between the imposed S/N condition, smoothing radii, and the ability to unveil true X-ray diffuse structures at spatial scales greater than the smoothing radii all over the field of view (FOV; see Figure 4). The units of the resulting flux maps are photons cm^{-2} s^{-1} arcsec^{-2}.

For subband images in the soft (0.5–1.2 keV), medium (1.2–2.5 keV), hard (2.5–7.0 keV), and total (0.5–7.0 keV) energy ranges, we adopted a different smoothing strategy. We decided to smooth subimages using the same set of radius kernels computed to achieve a given S/N in the band with poorest photon statistics. We adopted S/N ~ 16 to avoid smoothing radii becoming too large, with this condition relaxed at the borders of the detector. For the rest of the bands, smoothing was performed by fixing the smoothing radii map to that of the soft band via the optional parameter FIXED_RADIUS_MAP_FN. As the medium and hard X-ray bands have better photon statistics, the significance of such maps reaches higher S/N than in the soft band. In this way, we guarantee that the adopted S/N is always achieved for the rest of the energy band maps, as well as ensuring that the spatial scales of the maps are adequate for construction of hardness ratio (HR) maps.

3.1. The X-Ray Source Wing Diffuse Contribution

Based on the smoothing considerations presented in Section 3, we are able to estimate the contribution to diffuse emission produced by photon events in the extreme wings of sources that were not adequately excluded by the computed masked regions. To do this, we applied the same smoothing constraints used for the diffuse maps to the source wing diffuse maps of Figure 3 (right panel). The TARA_SMOOTH routine was fixed to radii computed for the flux diffuse emission at S/N $\geqslant$16.

In the left panel of Figure 5 we show the resulting diffuse wing emission contribution for ObsID 10951. The emission peaks at $\log(f_X) = -8.89$ photons cm^{-2} s^{-1} arcsec^{-2}, at large off-axis angles as a consequence of ill-constrained source + readout streak emission models related to the intense diffuse X-ray stellar source Schulte #5 (see Section 3.1). In order to quantify such possible contributions over the entire set of the observations, we computed the diffuse wings/total emission ($f_{\rm wings}/f_{\rm diffuse}$) maps to identify possible spatially resolved wing contamination zones. In the right panel of Figure 5, we can assert that, except for the very edges of the observation FOV, diffuse wing source contamination remains, in media, under 6% over the FOV.

Next, we computed the median ratio of the $f_{\rm wings}/f_{\rm diffuse}$ contamination for each of our observations. In media, these values, illustrated in Figure 6, range between 1% and 10%.

---

[13] These tasks are not part of the public AE software and were kindly shared by Dr. Patrick Broos of Penn State University's astrophysics group.

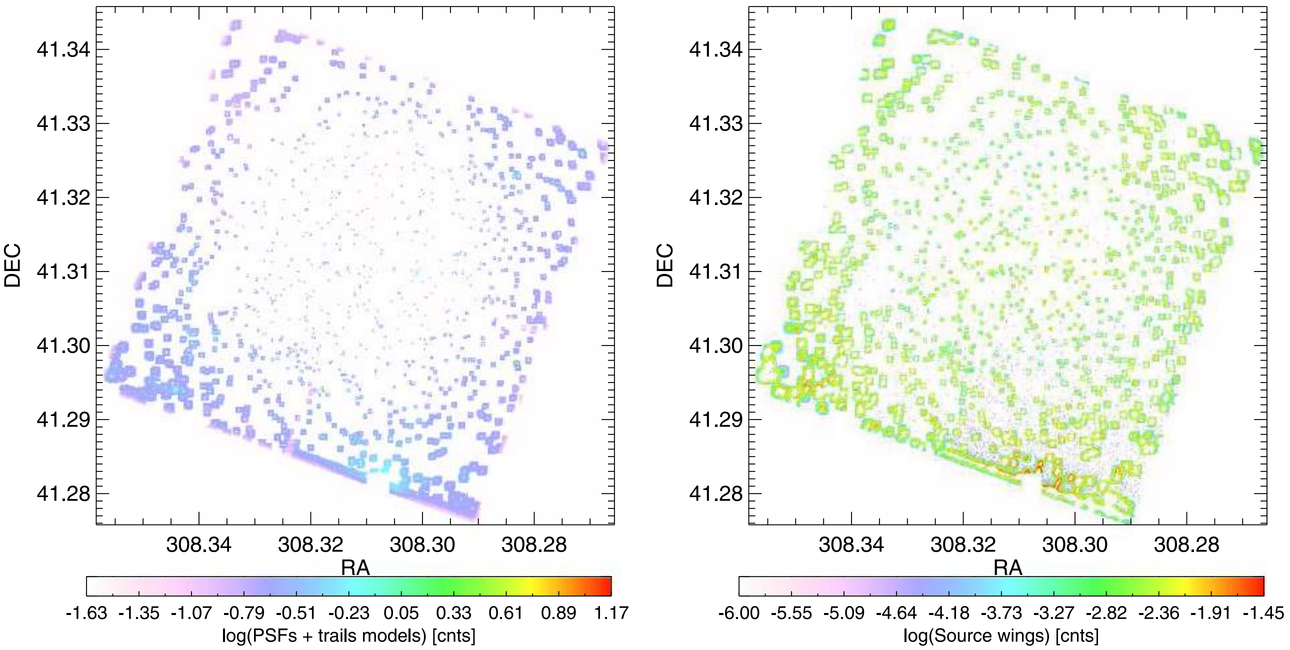

Figure 3. ObsID 10951, illustrating the treatment of point sources and their exclusion from diffuse emission maps. The same analysis was applied to the whole set of observations. Left: the source PSF and readout streak intensity models that were computed on the list of detected sources in the observation. Right: the residual PSF wings image, which was computed as the difference between the observed source count image and the source+streak intensity models (left panel). Scale bars of both panels show the intensity range in which the image spans.

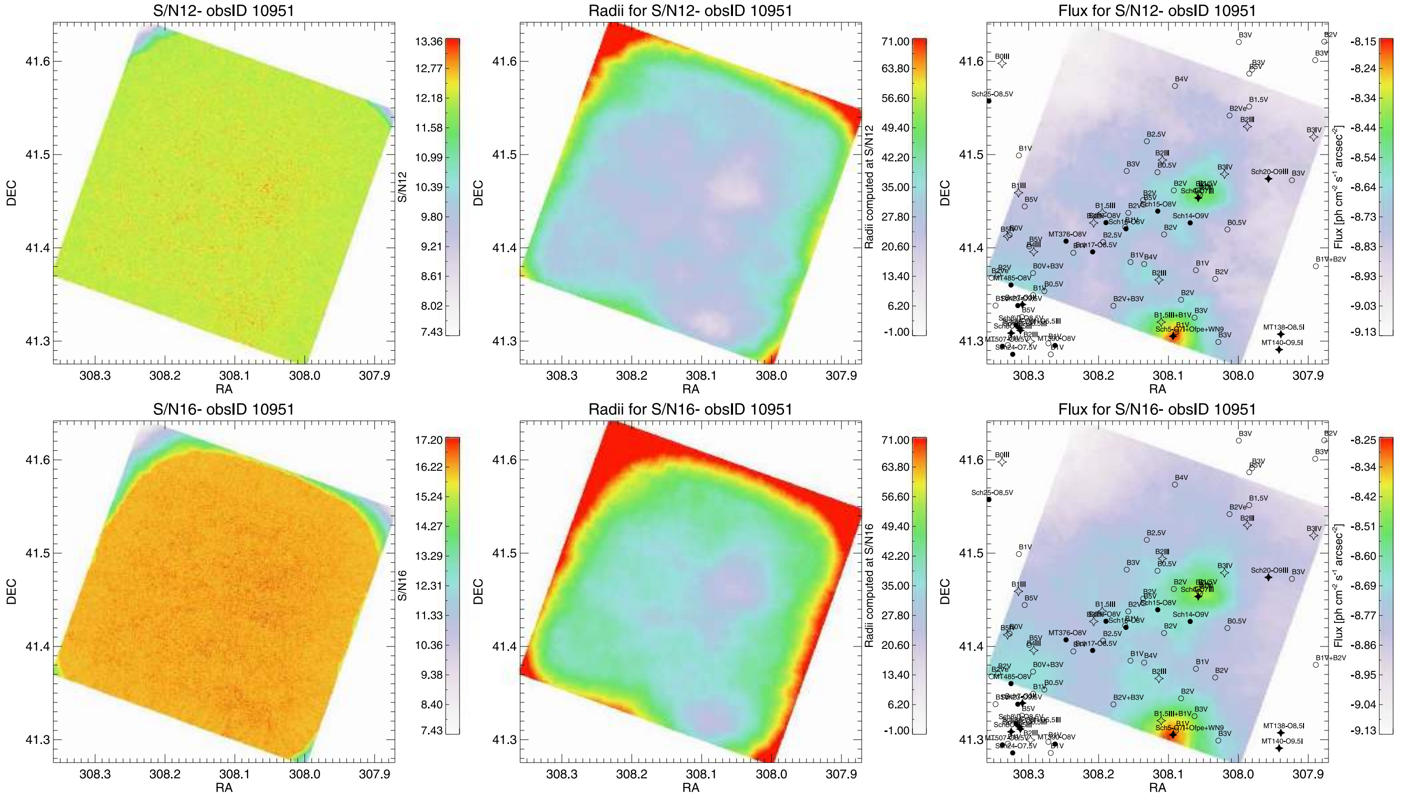

Figure 4. Exemplification of the procedure for ObsID 10951. Left panels: the S/N significance map computed at the imposed condition of S/N = 12 and 16, respectively. Middle panels: the top-hat radius computed to reach the imposed S/N condition. Up to the borders of the observation, the top-hat radii increase as much as necessary to achieve the S/N, although once off the detector the signal falls to zero and can reduce the final S/N below the desired threshold. Right panels: X-ray diffuse emission flux (photons cm^{-2} s^{-1} arcsec^{-2}) in the 0.5–7.0 keV energy range computed at S/N ∼ 12 and 16, respectively. Note that the peak of emission changes slightly for different S/N owing to the different binning, but by just 0.1 dex, or roughly 25%. At the limit of detection of the diffuse emission of $\log(F_X) \approx -8.64$ or -8.69, for S/N = 12 or 16, respectively, the difference is only 0.05 dex, or about 11%. Black filled-star symbols indicate the evolved massive stars with conspicuous X-ray emission; open star symbols refer to evolved massive stars without X-ray emission; black filled and open circles indicate main-sequence massive stars, with and without detected X-ray emission, respectively. The list of massive stars in Cygnus OB2 was taken from Wright et al. (2015b).

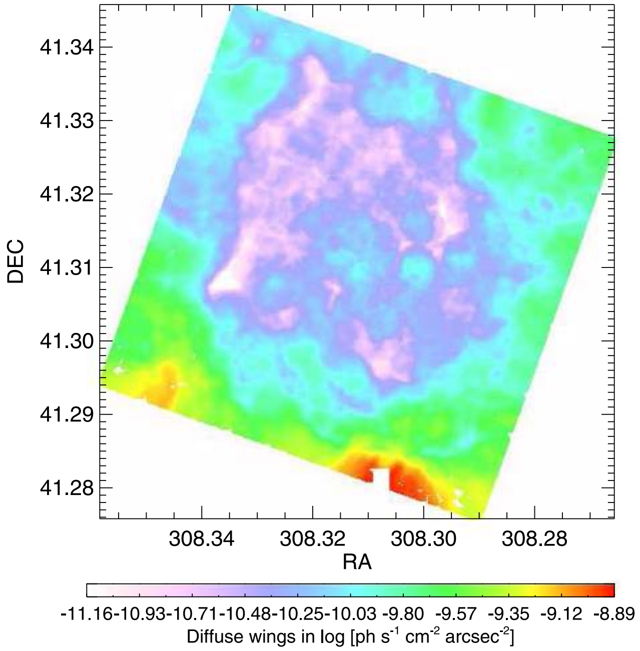

Figure 5. Exemplification of the procedure for ObsID 10951. Left: source wing diffuse contribution in the 0.5–7.0 keV energy range computed using fixed smoothing radii for S/N $\geqslant$ 16 in the full band. Right: the ratio of wings to total diffuse emission has a maximum contribution of 0.24, which lies at the border of the map. The median contribution from wings all over the image is about 6%.

However, there are some regions in which the ratio $f_{\rm wings}/f_{\rm diffuse}$ peaks at over 50% (ObsIDs 10952, 10953, 10956, 10957, 10958, 10964, 10969, 10970, and 10971). This occurs only for some intense sources located at large off-axis angles, or at the chip borders of the observations because of readout streak events or because the source PSF itself cannot accurately be modeled. These high ratios do not inconvenience our diffuse analysis at all, as they correspond to very small fractions (typically $\leqslant$4%–6%) of the map areas. We avoided these parts of observations in the diffuse X-ray analysis and instead used observations in which the same sky region appears close to on-axis, where the masked model describes adequately the local PSF of the sources.

4. X-Ray Hardness Ratio Maps

The construction of X-ray HR maps is a useful method of getting a first-order approximation of the spatial energy distribution of X-ray photons without losing spatial resolution. We produced (count-rate) maps in soft (S; 0.5–2.5 keV) and hard (H; 2.5–7.0 keV) X-ray bands and computed the HR as the ratio of the difference to the sum, i.e., (S − H)/(S + H). In this way we are able to discern soft and/or hard features in the diffuse X-rays regardless of their relative intensity. All HR maps were computed from maps that were smoothed using the top-hat method, but considering the fixed smoothing radius computed for an S/N $\geqslant$ 16 in the soft band (see Section 3 for a full explanation). We thus avoid false diffuse structures that would appear as a result of differences in the radii of the maps. HR maps were constructed for the entire set of observations in the survey (see the Appendix).

Figure 7 shows that softer diffuse emission follows the spatial distribution of massive stars from Wright et al. (2015b), even in those cases where massive stars do not emit significant X-rays themselves. As we discuss further below, the sensitivity of the HR maps highlights small changes in the energetics of the diffuse X-ray emission, providing clues about the impact of massive star stellar winds on the spectral energy distribution of the diffuse X-ray gas, even in those regions bereft of bright X-ray sources or with high ISM density.

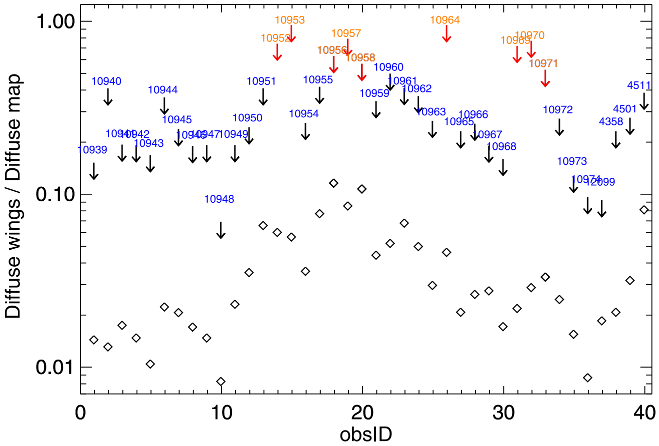

Figure 6. Downward-pointing arrows indicate maximum contributions of source wings to diffuse emission (see text for details). Red arrows indicate observations that are likely to be affected by gas and dust scattering processes related to the intense emission from Cygnus X-3. Black diamonds correspond to the median ratio of the wings to diffuse emission for the entire FOV of each observation.

The natural explanation for what we are seeing is that evolved massive stars in the region fill the volume of space between the massive stars with the summed contribution of hot shocked stellar winds. Eventually, these encounters drive a slow shock into the ISM, which contributes to the excitation of the observed Hα emission and, via the presence of dense neutral gas and/or dust structures, absorbs and reemits radiation in X-rays (see Section 7 for discussion).

However, in Figure 8 we find that not all HR values in the maps are descriptive of the energy of diffuse X-ray emission from shocked gas, and in those places where the diffuse emission is undetected, or absent, the extragalactic X-ray

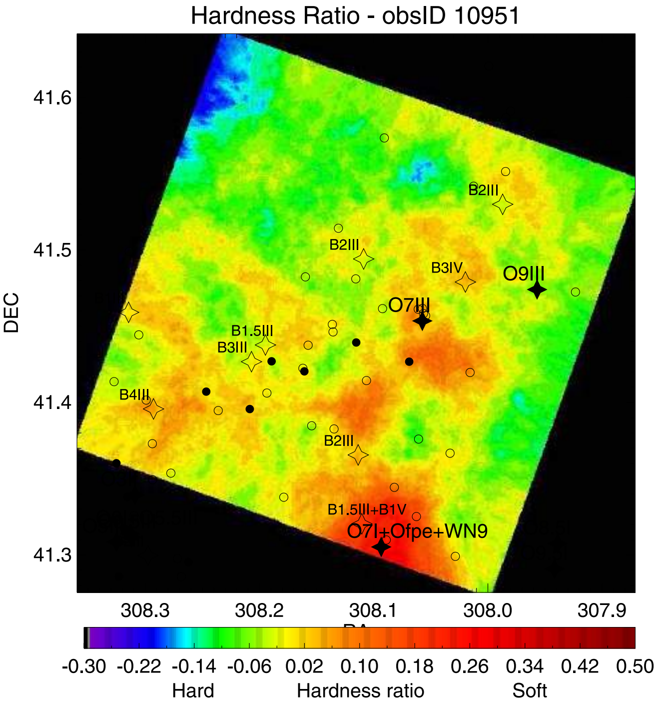

Figure 7. Exemplification of the HR analysis for ObsID 10951. The scale color bars show the range in HR that the image spans. Black filled and open star symbols indicate the evolved massive stars with and without intrinsic X-ray emission, respectively (from Wright et al. 2015b). Filled and open circles indicate MS massive stars, with and without intrinsic X-ray emission, respectively. Note that the diffuse gas follows the spatial distribution of the massive stellar population, regardless of whether they are strong X-ray emitters. The entire set of HR maps is shown in the Appendix.

background also appears to play a role in some cases (see Section 4.1).

4.1. Hardness Ratio of the Background

A serious difficulty in characterizing the diffuse emission energy distribution using HR maps concerns the problem of where the background becomes dominant and how to estimate a typical HR value for it. We make an initial estimation by searching for X-ray observations (or places in Cygnus OB2) in which X-ray diffuse emission appears to be absent (e.g., ObsID 10973 in Figure 20 of the Appendix). In this observation, no massive stars are in the FOV, and it is also unaffected by background scattering of X-rays from Cygnus X-3.

We computed the HR energy distribution of the smoothed background for the entire FOV of ObsID 10973, finding that it peaks at -0.16 ± 0.06. We have simulated a set of power-law emission spectra that adaptively constrains the observed HR values on this map. Typical Γ indexes range from 1.0 to 1.3, which agree with the expected spectral index for AGNs. In fact, this estimate of the hard X-ray background is known as the "X-ray background hardness problem" and originates from obscured AGNs, as discussed by May & Keel (2008). This problem refers to the cumulative contribution to the background of hard (energy $\geqslant$3 keV) emission from discrete unresolved sources (AGNs), each one emitting below the detection threshold of the observation. More precisely, for the total of ~1450 background X-ray sources in the Cygnus OB2 survey (Kashyap et al. 2023), we found the extragalactic contribution to be consistent with an $N_{\rm H}$ absorption of $\approx$2.0 $(\pm 0.09) \times 10^{22}$ cm^{-2} and a power-law Γ index of 1.3($\pm$0.05) (Flaccomio et al. 2023), which agree with typical HR $\leqslant -0.1$ values for AGNs.

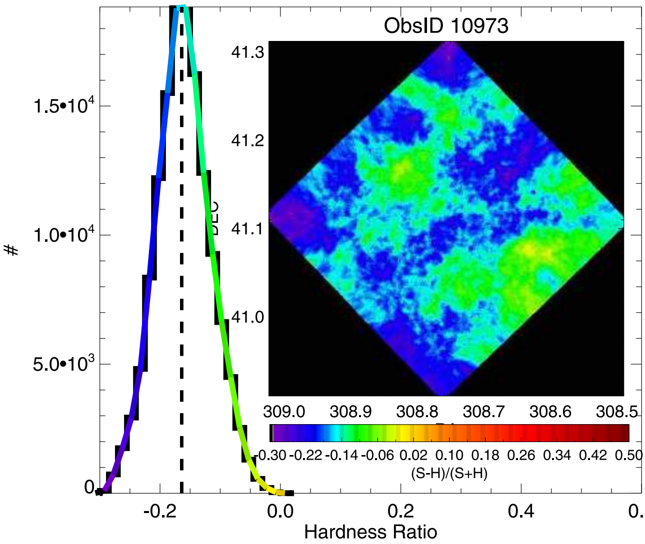

Figure 8. HR histogram for ObsID 10973. No obvious Cygnus OB2 X-ray diffuse emission was seen in this observation (see middle right panel of Figure 21 in the Appendix), so that the observed HR corresponds to that of the background emission. Colors in the histogram correspond to those of the color bar of the image. The peak of the HR distribution is about −0.16 for a 1σ of 0.06.

In summary, hard unresolved AGNs do not play a major role in the typical HR of the local diffuse emission, and its hard contribution appears homogeneous across the field of the observation (see HR map of ObsID 10973). This last conclusion agrees with the detailed analysis of the absorption along the line of sight of this region, which was independently computed and extensively discussed for the foreground, member, and extragalactic X-ray source populations (Flaccomio et al. 2023).

4.2. Dust Scattering from Cyg X-3 Emission

Cygnus X-3 is known to be a γ-ray source located in the background at a distance of 7.4 ± 1.1 kpc (McCollough et al. 2016), more than five times farther away than the Cygnus OB2 stellar association itself. Its radiation in X-rays is essentially hard ($\geqslant$3.5 keV; Koljonen et al. 2010), although in the soft (0.5–2.0 keV) X-ray band it is intense enough that it could mask any prominent diffuse structure in the vicinity of the line of sight, even when the source PSF has been masked at radii 1.5 times larger than the 99% encircled energy fraction (EEF). We have attempted to mitigate the influence of Cyg X-3 by disentangling hard and soft X-ray emission through the HR coded image, allowing us to reduce the impact of scattered photons, as well as to explore how far the scattering extends.

In six of the 40 X-ray observations of the survey, the scattering halo around Cyg X-3 was observed, either totally or partially, namely in ObsIDs 10939, 10940, 10964, 10969, 10970, and 12099. In Figure 9 we show the HR radial profiles and the smoothed images. As scattered radiation is dominated by hard photons, even harder than expected from the unresolved AGN background radiation, the peak of the HR reaches very negative values at the center, with HR ≈ -0.8. However, as the intensity decays with the inverse square of the radial distance (r^{-2}), at larger distances the influence of scattered X-ray photons from Cyg X-3 decreases to the typical

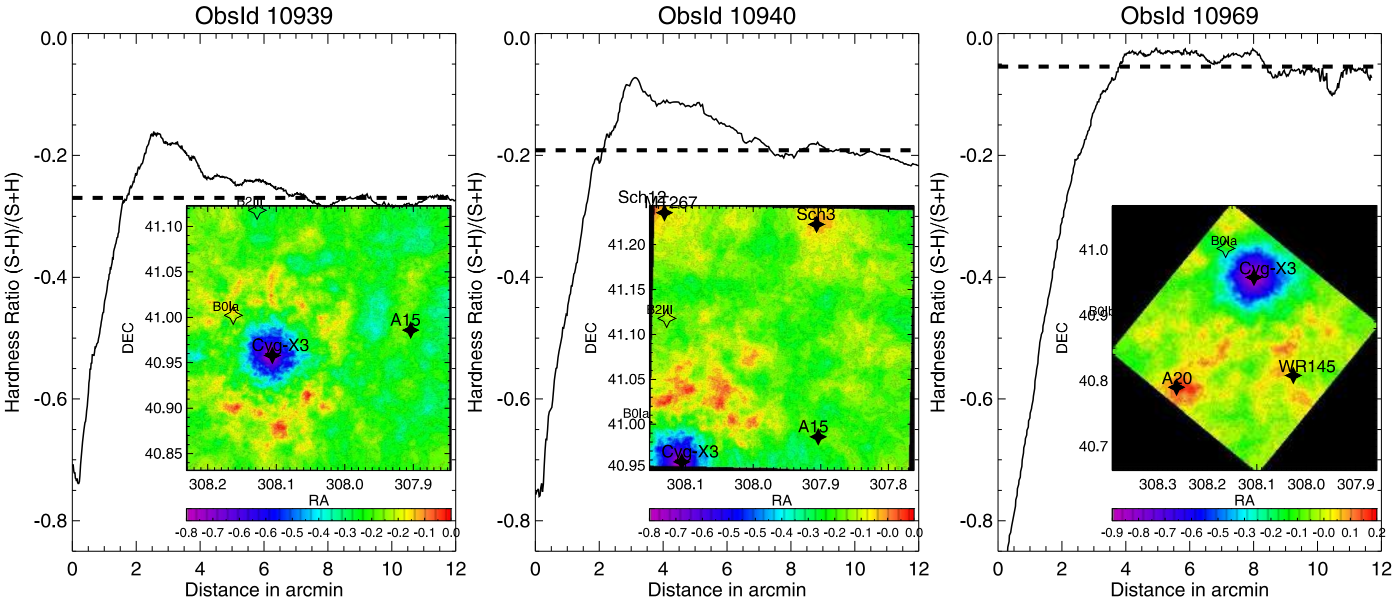

Figure 9. Cyg X-3 HR radial profiles of HR maps. Diffuse scattering extends to typical HR $\approx -0.14 \pm 0.07$, where in the worst case it drops to the level of the ambient Cyg OB2 HR at a radial angular scale of ≈8′. Beyond this range we consider the influence of Cygnus X-3 scattering on the diffuse X-ray emission to be negligible.

HR of the background (HR_{bkg}). At such a distance the radial profile becomes flat. On average, for all the observations we estimated that the HR_{bkg} levels off at large radial distances from Cyg X-3 at -0.14 ± 0.07, which is consistent with the value obtained in Section 4. The typical scattering halo of Cyg X-3 extends to a radius of about ∼8′.

We note the existence of some softer substructures (HR $\geqslant 0.05$) surrounding Cyg X-3, which are probably due to scattering from dust clouds along the line of sight to Cygnus X-3 (McCollough et al. 2013). Otherwise, HR values below -0.1 cannot realistically be considered part of the diffuse X-ray emission, as temperatures are required to be above 7 keV, which is unconstrained for the limited energy range of the observation. In any case, besides the poor photon statistics in such bands, HR values of ≈ -0.1, or harder, would be better described by a simple power-law emission model with spectral index $\Gamma = 1.7$ or lower (Corral et al. 2011). Hereafter, conservatively, reliable diffuse X-ray emission patterns in the HR maps would be considered for those HR values larger than ≈ -0.1.

5. Large-scale Diffuse X-Ray Map

The morphology and energetic large-scale appearance of diffuse X-ray emission in the Cygnus OB2 association are shown in the left panel of Figure 10. It is a mosaicked, point-source-removed image in the 0.5–7.0 keV energy range. Similar images were also made in three discrete energy bands: soft (0.5–1.2 keV), medium (1.2–2.5 keV), and hard (2.5–7.0 keV). These images include the complete set of ACIS-I observations of our survey and cover an area of about 1 deg^2 (see Section 7).

Mosaicking was performed using the Montage software to generate a list of images with corresponding WCS information. Before reprojection, we computed the individual emission levels required to match overlapping images. To do this, we determined the average emission level of two or multiple overlapped observations and scaled each image to match this average emission level. In cases of multiple overlapped images, the average diffuse emission level was computed by equal weighting averages. While more complex overlapping functions (e.g., cubic splines) might be employed and can in principle work well to match background levels in overlapping observations with X-ray point sources, we found that spline smoothing functions at the faint X-ray diffuse emission levels that characterize the Cygnus OB2 observations can be numerically ill conditioned, producing biased spline coefficients, not only resulting in mismatched scaling at the borders of each observation but also producing fake large-scale structures.

In the process of obtaining a full-coverage diffuse X-ray emission map for the observed Cygnus OB2 region and accounting for all the issues that could affect the diffuse X-ray emission level, we still need to account for one other possible underlying contamination problem, which is the contribution from the unresolved population of low-mass stars, in the stellar mass regime in which our survey detection is incomplete.

5.1. Unresolved Stellar Population versus Diffuse X-Ray Emission

One of the major problems facing the detection of diffuse X-ray emission in SFRs is the underlying contribution from unresolved sources that individually give rise to counts that fall below the detection threshold of the region. Three different contributions are addressed separately:

1. *Background contribution.* Guarcello et al. (2023b) and Wright et al. (2023a) found that about 78% (6149/7924) of X-ray sources detected in the Chandra survey were classified as Cygnus OB2 members. For background objects (1304 sources classified), the contribution from undetected AGNs remains under the detection threshold all over the entire set of observations, as was computed at the center of our Cygnus OB2 region using a deeper (100 ks) observation (Albacete Colombo et al. 2007).

2. *Foreground contribution.* The case of undetected foreground stars is more controversial because they appear softer than that of the background sources (see Flaccomio et al. 2023), and so it is expected to be more difficult to distinguish

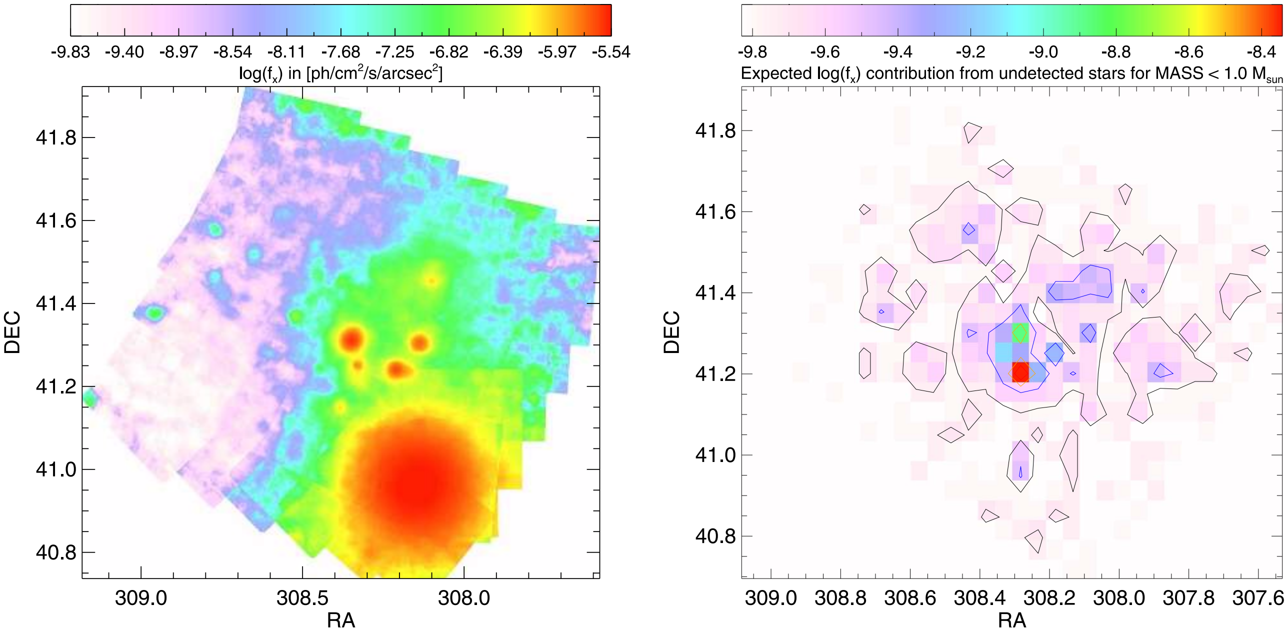

Figure 10. Left: the X-ray diffuse emission map for the full Cyg OB2 FOV in the 0.5–7.0 keV band. Right: contours in $\log(f_{\mathrm{unresolved}})$ indicating the intensity levels expected from the X-ray flux of unresolved stars.

from the spectrum of the diffuse emission. Based on the classification analysis of Chandra X-ray sources in the Cygnus OB2 region, we have identified ∼471 X-ray sources (∼6% of the total) as foreground stars (Kashyap et al. 2023). The stacked spectrum of all individually detected foreground stars toward the Cygnus OB2 region shows a soft thermal plasma emission with typical temperature and absorption of $kT = 0.77$ keV and $N_{\mathrm{H}}^{\mathrm{upper\ limit}} \approx 0.2 \times 10^{22}$ cm^{-2}, respectively (see Flaccomio et al. 2023). The total unresolved foreground stars are likely to have a similar spectral shape that could easily contribute to the observed soft diffuse X-ray emission. However, the clear anticorrelation between diffuse X-ray emission and observed colder gas−dust structures in the Cygnus OB2 association (see discussion in Section 7) suggests that the soft diffuse emission we detected is mainly associated with the Cygnus OB2 region. Alternatively, we used the investigation of Getman et al. (2011), which estimates a star foreground unresolved population of 200,000 toward Carina (2.3 kpc and area ∼ 1.42 deg^2). By scaling to the Cygnus OB2 region (1.4 kpc and area ∼ 0.97 deg^2), we estimate ∼18,500 unresolved foreground stars that would be in the projected area of the survey. They would emit at levels below the typical detection threshold of the survey of 6×10^{-5} counts s^{-1} (∼3 photons; Wright et al. 2023b). Hence, the total number of expected photons from unresolved foreground stars is less than or equal to $3 \times 18{,}500 \approx 56{,}000$ photons, or just ∼8% of the total of counts (∼710,000) observed in the entire 0.97 deg^2 Cygnus OB2 diffuse X-ray emission map.

3. *Stellar Cygnus OB2 contribution*. In order to compute the contribution to the observed X-ray diffuse emission level from unresolved low-mass stars belonging to the Cygnus OB2 region, we adopted the completeness limit for the survey from Wright et al. (2014b). With some small spatial variations (generally 10% or less in terms of flux), the X-ray luminosity completeness limit for our Cygnus OB2 survey area ranges from 50% at 1.4×10^{30} to 90% at 4×10^{30} erg s^{-1}. The actual percentage of stars detected is different for stars of different masses because the X-ray luminosity distribution is mass dependent. For the entire survey area the completeness is 50% at 0.6 $M_\odot$ and 90% at 1.3 $M_\odot$ (Wright et al. 2014b). For our purposes, the X-ray luminosities of stars were computed by adopting the X-ray conversion factor (CF), i.e., the ratio between unabsorbed flux (f_{ua}) in erg to the absorbed flux in photons (f_{abs} [photons]), which corresponds to a value of 5.4×10^{-9} erg photon^{-1} (see Flaccomio et al. 2023).

We assumed that the X-ray luminosities of the stellar population of Cygnus OB2 stars at masses in which our survey is essentially complete are the same as those of stars of the same mass in the ONC. We then used the results of COUP, which is essentially complete at all masses above 0.3 $M_\odot$ (Feigelson et al. 2005; Getman et al. 2005; Preibisch et al. 2005), to infer the signal from stars in Cygnus OB2 with masses below 1.0 $M_\odot$, for which we are complete to a level of about 85%.

The expected X-ray luminosity contribution for stars with masses in the range 0.3–1.0 $M_\odot$ per star in the ONC is $L_{\mathrm{uc}}^{\mathrm{ONC}} \sim 5.8 \times 10^{30}$ erg s^{-1}. At the distance of Orion (d ∼450 pc), and accounting for our CF (erg photon^{-1}), we obtained the expected flux per detected star, $f_{\mathrm{uc}}^{\mathrm{ONC}} = 4.5 \times 10^{-5}$ photons s^{-1} cm^{-2} star^{-1}). For COUP stars with a visual extinction $A_v \leqslant 5$ mag and masses below 1.0 $M_\odot$, we get a total population of 84 stars. Applying the same restriction for the Cygnus OB2 members, we find 786 stellar members with masses in the range 0.3–1.0 $M_\odot$. This implies that Cygnus OB2 is ∼9.2 times more massive than Orion for the same mass range. By adopting a distance of 1450 pc to Cygnus OB2, the total X-ray contribution for unresolved stars in the range 0.3–1.0 $M_\odot$ and over the entire observed area (∼1 deg^2) is $f_{\mathrm{uc}}^{\mathrm{CygOB2}} \sim 4.6 \times 10^{-6}$ photons s^{-1} cm^{-2} star^{-1}. In the left panel of Figure 10, we illustrate the Cygnus OB2 source density map binned at 0.05 deg^2, weighted by the expected X-ray flux contribution of undetected stars. Thus, the expected flux, $f_{\mathrm{uc}}^{\mathrm{CygOB2}}$, should be divided by the unit of area adopted for binning, dens_area = $(0.05 \times 3600)^2$ stars arcsec^{-2}. Finally, for each detected low-mass star the expected X-ray flux emission from unresolved stars per arcsec^2 ($f_{\mathrm{X}}^{\mathrm{uc}}$) is

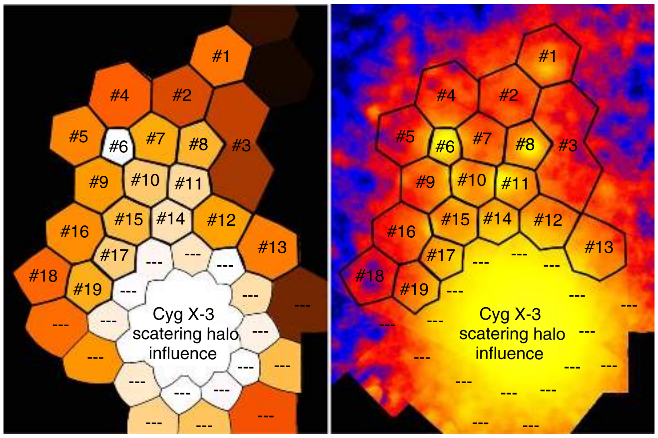

Figure 11. Left: tessellated X-ray surface brightness of the Cygnus OB2 region. The achieved S/N is 60, and regions were computed to perform spatially resolved X-ray spectral fitting. Regions labeled with dashed lines were not taken into account owing to the influence of the background-scattered X-ray radiation from Cyg X-3 (see discussion in Section 4.2). Right: diffuse X-ray mosaic events used for spectral extraction.

$f_{\rm uc}^{\rm CygOB2}$/dens_area $= 1.4 \times 10^{-10}$ photons s^{-1} cm^{-2} arcsec^{-2}, i.e., ($\log(f_{\rm X}^{\rm uc}) = -9.84$). Note that the peak of the expected X-ray flux contribution is $\log(\max(f_{\rm X}^{\rm uc})) = -8.34$ photons s^{-1} cm^{-2} arcsec^{-2}, and this occurs only in a single region of 0.05 deg^2 centered at R.A. = 308.3 deg and decl. = 41.2 deg (Figure 10, right panel). However, this value is overestimated because we made use of a completeness function computed from 120 ks simulations (Wright et al. 2023b), while at this central position our survey has a nominal summed exposure of ∼220 ks, leading to a deeper source detection threshold.

With this estimation, and at the same time by comparison with our X-ray diffuse emission map, computed using the same spatial binning of 0.05 deg^2 (see Figure 10, right panel), the detected X-ray diffuse emission patterns in the survey are above $\log(f_{\rm X}) \approx -8.2$. Thus, the contribution from the unresolved stellar population, in the worst case, remains a factor 2.5 fainter than the observed emission. For the vast majority of the survey area, it is at least an order of magnitude lower, confirming that detected X-ray diffuse emission structures are real and not affected by the contribution of X-ray emission from undetected low-mass stars of the region.

6. Spectral Analysis of Diffuse X-Ray Emission

X-ray spectral fitting of diffuse emission is a difficult undertaking and requires sufficient X-ray photons to provide meaningful constraints on the X-ray spectral model parameters. The most straightforward procedure is to increase the source extraction areas to gain larger S/Ns. To this end, we tessellated the whole image mosaic in the 0.5–7.0 keV band to achieve surface brightness regions with S/N greater than 60. Figure 11 shows the tessellate-generated image made using the weighted Voronoi tessellation (WVT) binning code (Diehl & Statler 2006). These tessellated regions can be readily translated into region files and used to extract events within CIAO. In order to avoid the contamination produced by the bright background-scattered X-ray halo of Cyg X-3, all tessellated regions within an 8′ radius of its position (R.A. ≈20:32’, decl. ≈ +40:57’) were excluded from the spectral analysis. The choice of this distance was discussed earlier in Section 4.2. However, for some tessellated regions, even beyond 8′, the fractional X-ray contribution would produce marginal contamination in the diffuse X-ray spectra. We account for this issue in the spectral model fitting and subtract residual Cyg X-3 signal from the total 0.5–7.0 keV diffuse emission. The spatially resolved spectral fitting models and parameters are presented in Table 1.

The extraction of the X-ray spectrum for each tessellated region was achieved by using the specextract CIAO task from the respective diffuse event files. All spectra were properly weighted by the appropriate calibration files (the so-called ARFs and RMFs), which account for the many partially overlapping ObsIDs. Background X-ray spectra were computed by using “stowed calibration events files.” All X-ray spectra were grouped to reach a minimum S/N per bin of 1, which produce unbiased best-fit values for the fitting procedure (Albacete-Colombo et al. 2023).

For spectral fits, we used a suite of XSPEC spectral models (Arnaud 1996) to adequately account for possible combinations of emission components affected by equivalent hydrogen NH absorption column. The latter was included using the TBABS (Tuebingen−Boulder, TB) model (Wilms et al. 2000), which is composed by a combination of N(HI) (atomic hydrogen) and 2 N(H2) (molecular hydrogen). We tested the differences in the use of thermal emission models such as “PSHOCK” (PS), which is an averaged-abundance plane-parallel shock in noncollisional ionization equilibrium (NEI), and combination of “APEC” (AP) collisional ionization equilibrium (CIE) plasma models (Smith et al. 2001).

Unfortunately, the statistics of the spectra impose a limitation on the number of spectral models and free parameters that can be usefully constrained. We initially used the PS model to fit the softer (“supersoft”—SS) component (kT1), which gives short ionization timescales (from $\tau_u \sim 10^{-10}$ to 10^{-11} s cm^{-3}), implying a low-density highly nonequilibrium plasma (NEI). This interpretation supports intense and recent stellar winds and ISM shock interactions (Smith & Hughes 2010). Otherwise, “soft” (S) and “moderate” (M) energies were successfully described by two AP plasma models (kT2 and kT3) that adequately fit the observations for intermediate temperatures of each tessellated region. Finally, a fourth “hard” (H) CIE plasma model (kT4) accounts for background nonresolved AGN—faint and hard—X-ray emission. Such a hard thermal component was able to match most of the hard diffuse emission, even though AGNs are expected to be dominated by NT emission and are usually well modeled with power-law spectral shapes. However, the use of a thermal plasma spectral shape (kT4) may also be fitting more than just the unresolved AGN emission (Townsley et al. 2011a). Several attempts with simple (1T or 2T) models do not adequately fit the shape of the diffuse X-ray spectra, so we adopt a 4T combined model for spectral fitting, which is written with an XSPEC expression:

$$TB_1 \times PS_1 + TB_2 \times AP_2 + TB_3 \times AP_3 + TB_4 \times AP_4. \qquad (1)$$

Models with variable abundance, e.g., “VPSHOCK” and “VAPEC,” were not used, as the number of free channels in the spectra is insufficient to discriminate adequately for differential abundance contributions from single elements. Otherwise, the fixed solar metal abundance pattern with scalable metallicity, Z, was not allowed to go below solar ($Z = 1$), as it is unlikely that massive star winds could produce subsolar plasma abundances (Strickland & Stevens 1998; Pittard & Parkin 2010). In fact, sometimes we slightly improved the goodness of the fit by

Table 1
Spectral Model Parameters of Diffuse X-ray Emission

Reg. No.	Model	N_H ($\times 10^{22}$ cm^{-2}) Diffuse/Bkg.	kT (keV) Diffuse/Bkg.	Norm. (cm^{-3})	Z ($Z_\odot$)	Flux ($\times 10^{-12}$ cgs) Diffuse/Bkg.	L_X ($\times 10^{33}$ cgs) Diffuse/Bkg.
1	3T/bkg	0.34−0.58−1.37/2.6	0.11−1.01−0.48/44.5	0.26	1.3	6.07/3.13	1.52/0.78
2	3T/bkg	0.50−0.59−1.53/2.6	0.10−0.76−0.42/34.4	0.40	1.7	10.9/2.99	2.74/0.75
3	3T/bkg	0.46−1.05−1.67/5.8	0.11−1.24−0.50/[64.0]	0.56	3.4	29.2/9.12	7.34/2.29
4	3T/bkg	0.33−0.50−1.35/1.6	0.09−0.31−1.23/[64.0]	0.11	1.7	5.80/2.75	1.46/0.69
5	3T/bkg	0.44−1.04−1.48/5.6	0.12−1.22−0.47/56.1	0.23	3.7	11.79/3.01	2.96/0.75
6	3T/bkg	0.57−1.00−1.05/[10]	0.13−0.56−1.21/13.7	0.13	2.1	6.77/1.76	1.71/0.44
7	3T/bkg	0.18−0.66−0.98/2.7	0.08−0.91−0.42/[64.0]	0.23	1.4	3.34/2.13	0.85/0.53
8	3T/bkg	0.33−0.80−1.39/4.6	0.11−0.38−1.02/57.3	0.12	2.1	7.25/1.86	1.82/0.46
9	3T/bkg	0.29−0.76−1.44/2.8	0.11−0.39−1.08/[60]	0.11	2.1	4.26/2.32	1.07/0.58
10	3T/bkg	0.45−1.23−1.38/4.5	0.13−1.21−0.46/43.3	0.14	1.6	7.44/2.74	1.87/0.68
11	3T/bkg	0.44−1.00−1.36/4.2	0.10−1.11−0.51/42.7	0.44	1.9	6.69/2.37	1.68/0.59
12[a]	2*T* / Cyg X-3+bkg	0.49−0.97/1.7−2.7	0.12−0.45 /11.4−[64]	0.25	3.8	9.31/3.15	2.34/0.79
13[a]	2*T* / Cyg X-3+bkg	0.40−0.71/2.9−2.6	0.11−0.53/10.8−[64]	0.26	1.8	9.30/2.87	2.33/0.72
14[a]	2*T* / Cyg X-3+bkg	0.52−1.60/2.9	0.10−0.41/61.8	0.27	1.1	9.96/3.16	2.50/0.79
15	3T/bkg	0.43−0.74−0.83/2.6	0.10−0.27−5.7/39.8	0.26	3.8	5.25/2.56	1.32/0.64
16	3T/bkg	0.38−0.80−1.81/3.4	0.11−0.38−0.68/7.8	0.16	1.8	5.97/5.02	1.51/1.26
17[a]	2*T* / Cyg X-3+bkg	0.50−1.86/2.6	0.11−0.51/10.8	0.50	1.7	5.26/2.90	1.33/0.72
18	3T/bkg	0.34−0.98−2.38/4.1	0.13−0.44−1.21/27.4	0.04	1.7	5.46/2.38	1.37/0.59
19[a]	3*T* / Cyg X-3+bkg	0.38−1.26−1.61/2.6	0.11−0.32−1.26/[64]	0.29	3.9	14.6/2.66	3.67/0.66

Stacked	Model	N_H Components	kT Components	Norm.	Z	Flux	L_X	% Diff.
SS	Supersoft	0.43 ± 0.09	0.11 ± 0.01	2.53	1.3	60.4 ± 7.5	15.2 ± 1.9	37 ± 3
S	Soft	0.80 ± 0.22	0.40 ± 0.08	1.79	1.8	75.1 ± 10.1	18.9 ± 2.7	46 ± 5
M	Moderate	1.39 ± 0.28	1.18 ± 0.18	0.43	3.1	31.0 ± 5.1	7.8 ± 1.3	17 ± 2
H	Hard	2.70 ± 0.42	45 ± 19	0.09	1.0	56.0 ± 16.7	14.1 ± 4.2	⋯
Diffuse	SS+S + M			4.76	[1.2]	166.7 ± 26.1	41.95 ± 6.6	100

Notes. The "bkg"—the hardest component of the diffuse emission spectra—refers to the contribution from unresolved AGN background emission. A thermal model approximation is sufficient to describe the hard emission (see text for discussion). Columns (5) (Norm.) and (6) (Z) refer to the normalization parameter and the abundance of the model, respectively. The presence of diffuse NT emission is addressed in Section 7. Both flux and luminosity were computed for the 0.5−7.0 keV energy range. The last column of the lower section of the table indicates the percentage of SS, S, and M contribution to the total diffuse X-ray emission.

[a] Refers to spectra affected by Cyg X-3 scattered photons, which were also modeled by a thermal component.

allowing supersolar abundances, even if the actual abundance values were often not well constrained and/or eventually fixed. The spectral analysis was performed in an interactive way, with metallicity thawed, but carefully fitting in the restricted range of $Z = 1.0$–5.0.

For some tessellated regions (Nos. 12, 13, 14, 17, and 19; see Table 1), the fourth hard (kT4) component helps us to disentangle the marginal contribution of the diffuse background (∼9 kpc) scattering emission from Cyg X-3. In these cases, the absorption associated with the hard thermal component would be representative of a large total N_H absorption column, so it was initially set at 1.8×10^{22} cm^{-2}, but restricted in the fit to the range $(0.8–10.0) \times 10^{22}$ cm^{-2}.

The goodness of fit (χ^2/dof) obtained is generally acceptable (ranging from ∼1.0 to 1.1) for most of the tessellated regions. However, some cases of χ^2/dof ∼ 1.2–1.3 are probably associated with an ill-constrained emission model for scattered hard X-ray photons from the Cyg X-3 background radiation.

In Figure 12, we show six example X-ray diffuse spectra that exhibit different spectral characteristics. In Table 1, we give the best-fit spectral parameters for the diffuse X-ray emission tessellated areas. Not surprisingly, three independent absorption models shape the apparent diffuse X-ray brightness of the region. For the stacked spectrum we get absorption values N_H^1, N_H^2, and N_H^3 of 0.43×10^{22} cm^{-2} ($1\sigma = 0.09$), 0.80×10^{22} cm^{-2} ($1\sigma = 0.22$), and 1.39×10^{22} cm^{-2} ($1\sigma = 0.28$), respectively, and temperatures of the components kT$_1$, kT$_2$, and kT$_3$ of 0.11 ($1\sigma = 0.01$), 0.42 ($1\sigma = 0.08$), and 1.21 ($1\sigma = 0.18$), respectively. This is direct evidence of the existence of a wide range of multitemperature gas in the region. Otherwise, the hardest component is adequately described by a typical $N_H^4 \approx 2.7 \times 10^{22}$ cm^{-2} and a hard contribution from the unresolved AGN background population that can be represented by a ∼2.8−15 keV plasma.

Spectral analysis of the combined ("stacked") spectrum of the full region was performed using a four-temperature thermal input model. Results are consistent with those obtained from the averages computed for spatially resolved spectra. The total intrinsic diffuse X-ray luminosity is $L_X = 5.6 \times 10^{34}$ erg s^{-1} for the 0.5–7.0 keV energy range. As shown in Figure 13, the total diffuse spectrum is successfully reproduced by a mix of the supersoft (SS) + soft (S) + moderate (M) + hard (H) plasma emission models. Unfortunately, there are also some regions of SS emission away from the center of the Cygnus OB2 association that are too faint to construct tessellated regions for spectral extraction at S/N > 1.

In contrast with the first three thermal components (SS, S, and M), the H model appears highly absorbed (∼2.6×10^{22} cm^{-2}) and extremely hard ($kT > 15$ keV), as expected from the unresolved AGN background population and/or—for some cases—the scattered radiation from Cyg X-3. This hard component is then not part of the local diffuse X-ray emission of the

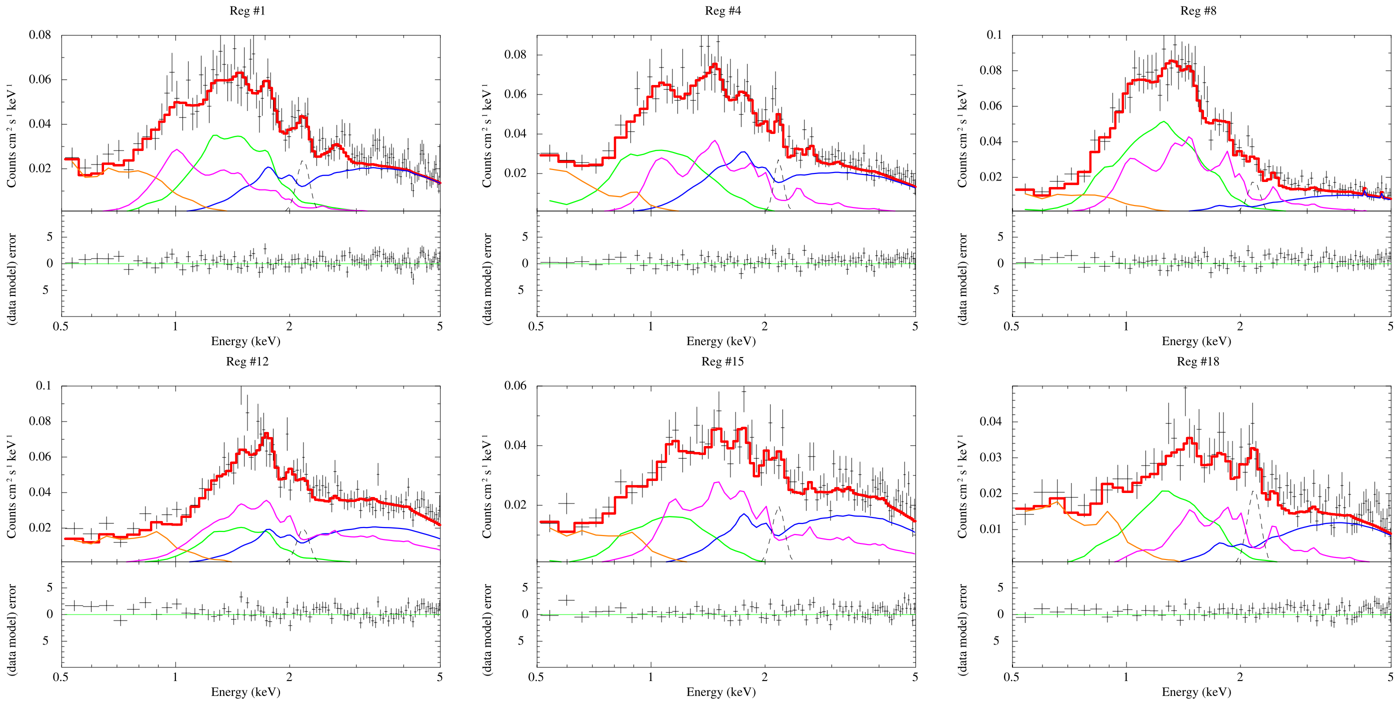

Figure 12. Sample of some tessellate spectra for region Nos. 1, 4, 8, 12, 15, and 18. Models that describe diffuse X-ray emission are indicated with red solid lines. The thinner colored lines represent the decomposition of the total emission into different models: supersoft (SS—orange), soft (S—green), moderate (M—magenta), and hard (H—blue). Note: black dashed lines correspond to the residual instrumental line at ∼2.1 keV from background stowed spectra, which has not be taken into account for the event/stowed background normalization (see 2.2 for discussion).

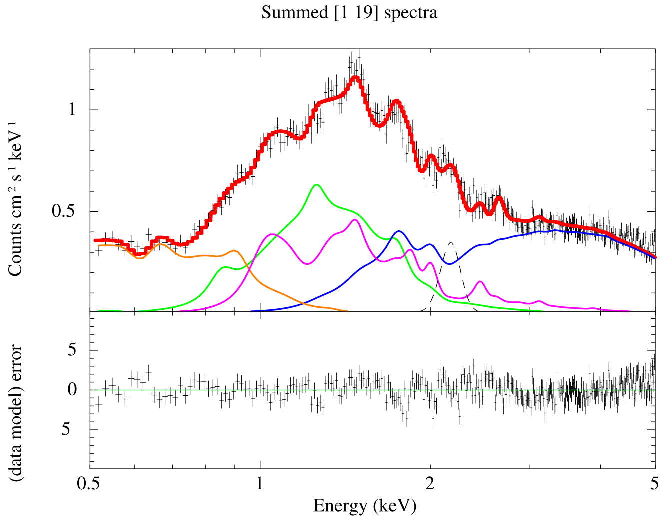

Figure 13. Stacked diffuse X-ray spectrum for the Cygnus OB2 region. The total (0.5−7.0 keV) diffuse X-ray fitted model (thick red line) has an intrinsic $L_{\rm tot}$ of 5.6×10^{34} erg s^{-1}. The total emission is decomposed into different models: supersoft (SS—orange), soft (S—green), moderate (M—magenta), and hard (H—blue).

region, so we have disentangled such a component to estimate a background X-ray luminosity of $L_{\rm X}^{\rm H}$ ($\sim 1.41 \times 10^{34}$ erg s^{-1}). Certainly, hard X-rays might originate in the Cyg OB2 association. In Section 7.2 we discuss plausible NT emission mechanisms present in the local diffuse X-ray emission of the region.

We consider the truly diffuse X-ray emission of the Cygnus OB2 region to be composed of the contribution from SS + S + M models, which have a total combined X-ray luminosity of $L_{\rm X}^{\rm diff} = 4.2 \times 10^{34}$ erg s^{-1} for the 0.5–7.0 keV energy range. The softer SS component is compatible with a temperature of 0.11 keV and a low absorption column of 0.42×10^{22} cm^{-2}, which appears spatially related to the shock interaction between winds from massive stars and the local ISM (see Section 7). Its relative contribution to the total X-ray diffuse emission of the region is ∼37% ($L_{\rm X}^{\rm SS} \sim 1.52 \times 10^{34}$ erg s^{-1}), although due to the scattered soft emission too faint for quantitative analysis mentioned above, the true SS flux could be larger. In fact, SS emission is just observed where absorption is low enough, being completely absorbed at other parts of the region. The S and M components, with respective temperatures of 0.40 and 1.18 keV, appear 2.8−3.2 times more absorbed (1.18×10^{22} cm^{-2} and 1.30×10^{22} cm^{-2}, respectively) than the SS emission. The S component contributes 46% ($L_{\rm X}^{\rm S} \sim 1.89 \times 10^{34}$ erg s^{-1}) and the M component 17% ($L_{\rm X}^{\rm M} \sim 0.69 \times 10^{34}$ erg s^{-1}) of the total diffuse X-ray luminosity of the region.

7. Discussion

This work has demonstrated, for the first time, the existence of true diffuse X-ray emission in the Cygnus OB2 stellar association. It is of interest to examine possible mechanisms responsible for the observed diffuse emission and its spatial morphology, which is probably related to a mix of different, thermal and/or NT, physical mechanisms acting separately, but sharing a single spatial region. In Figure 14 we show a global view of the diffuse X-ray emission that is dominated by a mix of soft (0.5–1.2 keV) and intermediate hardness (1.2–2.5 keV) X-rays, in agreement with three thermal contributions that we obtained from spectral analysis. The hard (2.5–7.0 keV) energy band is instead largely dominated by the background contamination (see Section 4.1) and/or, in some regions, scattered radiation from Cygnus X-3 (see Section 4.2).

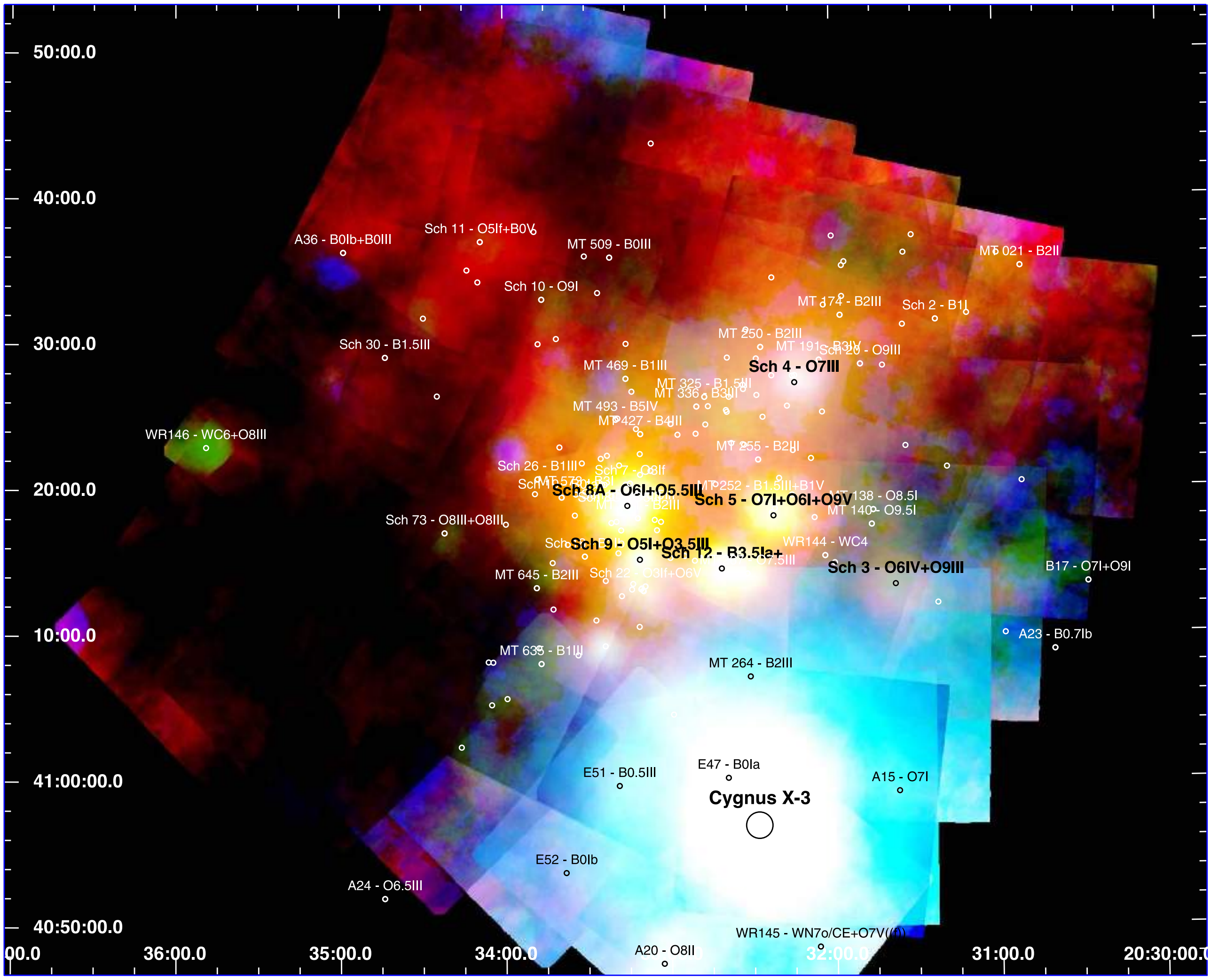

Figure 14. The Cygnus OB2 diffuse emission map in the 0.5–7.0 keV band. The full band is coded in color so that soft (0.5–1.2 keV) emission appears in red and medium (1.2–2.5 keV) emission appears in green, while hard (2.5–7.0 keV) emission appears in blue. Small white circles indicate the massive stellar content of the region. Names and labels indicate the evolved stars with more intense stellar winds. Names are omitted for main-sequence O- and B-type stars that have less massive winds. The X-ray mosaic intensity is logarithmically scaled, and the region shown is approximately 1.3 × 1.3 deg, with north up and east to the left.

7.1. Thermal Contribution to Diffuse X-Ray Emission

The diffuse emission closely follows the spatial distribution of massive stars (Wright et al. 2015b). The most widely accepted physical mechanism for production of diffuse hot gas is by multiple interactions of the winds from massive stars with the ambient ISM (e.g., Cantó et al. 2000). This kind of ISM–wind interaction occurs under the action of stellar wind momentum so as to produce low ISM densities, such that the X-ray diffuse gas would be characterized by high pressure (low ISM density) and high temperature. However, it is remarkable that the soft (0.5–1.2 keV) contribution, which is somewhat fainter than intermediate energy band emission, appears much more dispersed and also less confined at the locations of evolved massive stars. This result suggests that the cumulative influence of intense massive stellar winds acts to fill and heat the surrounding ISM, injecting enough thermal energy to drive outward via expanding turbulent diffusive motions of hot gas on scales of several parsecs, even in places absent of massive stars (Dwarkadas & Rosenberg 2013).

According to simple theoretical scaling approximations (Stevens & Hartwell 2003), part of the stellar wind kinetic energy is thermalized, so we can derive a simple estimate for the expected temperature of the shocked gas, $T_{\rm shock} \approx 1.3 \times 10^7 (v_w/1000)^2$ K, where v_w is the typical stellar wind velocity of massive stars in units of kilometers per second. For massive stars the stellar wind expansion obeys a β-law velocity, $v(r) = v_\infty(1 - R_\star/r)^\beta$, with $\beta = 0.8$ for supersonic winds (Pauldrach et al. 1986); thus, for distances greater than 10 times the stellar radius ($10R_\star \leqslant 0.01$ pc) the ratio $v_w/v_\infty \geqslant 0.95$, so v_w is well approximated with typical v_∞ values. The stellar terminal wind velocity of early O-type stars ranges from 900 to 2800 km s^{-1}, so gas temperatures would range between 1.0×10^7 K and 10.1×10^7 K, which is equivalent to energies of ~0.9–8.7 keV. While these energies are roughly consistent with what we observe, they should be considered as upper limits because $T_{\rm shock}$ here is computed as a purely radiative limit. In a more realistic description, it is expected that a fraction of energy released from the winds of massive stars deposits mechanical energy into the ISM.

The entire massive stellar content of the Cygnus OB2 region comprises (i) 25 evolved (of classes I, Ie, II((f)), III) massive stars of O type, plus 4 Wolf-Rayet stars; (ii) 28 evolved B-type stars of classes I, Ia, Ib, II, III, most of them characterized by slow winds and faint, or absent, intrinsic X-ray emission; and (iii) 113 O-type and early B-type stars on the MS (Wright et al. 2015c). The contribution to the total stellar wind energy L_w released by each star can be obtained according to the expression $3 \times 10^{35}\, \dot{M}_{-6}\, (v_w/1000)^2$ in erg s^{-1}, where $\dot{M}_{-6}$ is the mass-loss rate in units of $10^{-6}\, M_\odot\, \mathrm{yr}^{-1}$ (Cantó et al. 2000). We adopted individual mass-loss rates according to the Vink et al. (2001) formalism and terminal wind velocity assumption of $v_\infty = 2.6\, v_{\mathrm{esc}}$ (Lamers et al. 1995), which were computed by Rauw et al. (2015) for the entire massive star population of the region. The total L_w released by each one of these three groups separately is $\approx 1.3 \times 10^{38}$ erg s^{-1}, 6.6×10^{36} erg s^{-1}, and 1.3×10^{37} erg s^{-1}, respectively. The total stellar wind energy injected into the ISM of the region, from the entire population of massive stars, is then $\approx 1.5 \times 10^{38}$ erg s^{-1}, with the evolved O stars dominating.

At this point, it is interesting to estimate the kinetic-to-diffuse X-ray emission efficiency by computing the diffuse X-ray luminosity of the region. Early works based on the CWM have provided some reliable estimates for the X-ray diffuse emission in massive SFRs, e.g., R136 and NGC 3603 (Moffat et al. 2002), NGC 346 (Nazé et al. 2002), Rosette (Townsley et al. 2003), and Westerlund I (Muno et al. 2006). They have found that the diffuse X-ray luminosity in the broad band of 0.5–8.0 keV usually lies in the range (1–6) $\times$ 10^{34} erg s^{-1}. Such estimates indeed confirm the efficiency $L_{\mathrm{X}}^{\mathrm{diff}}/L_w \sim 2 \times 10^{-4}$, as predicted by Dorland & Montmerle (1987) through the investigation of dissipative mechanisms. Now, if we assume that the diffuse X-ray emission luminosity is entirely produced through wind shock–ISM dynamical interaction, the efficiency in Cygnus OB2 is $\eta \sim L_{\mathrm{X}}^{\mathrm{diffuse}}/L_w = 4.2 \times 10^{34}/1.5 \times 10^{38} = 2.8 \times 10^{-4}$, or about a factor $\sim$2 more efficient than in Westerlund 1 (Wd 1).

Next, we are able to estimate the diffuse X-ray luminosity via the CWM model. Such a model assumes that the bulk of the diffuse emission in the region is due to a hot plasma that exhibits relaxed, center-filled morphology with a lack of any obvious, measurable temperature gradients. We therefore considered the simple hypothesis of uniform, optically thin thermal plasma with a simple geometry, although the emission doubtless has a more complex structure in reality. As discussed in Section 4, thermal diffuse emission is an adequate description if we adopt diffuse emission regions with HR below -0.1. Figure 15 shows this diffuse emission with regions of harder emission removed.

The total mass of hot gas (HR $\geqslant -0.1$) in the region that emits in X-rays covers overly precise $\sim$35% of the total survey area of $\approx 0.97\ \mathrm{deg}^2$, which at the distance of 1450 pc to Cygnus OB2 corresponds to an area of 209.5 pc^2. This area is equal to a 14.5×14.5 parsec side (s_x) square. Because stellar wind–ISM interaction occurs in a 3D space, the observed bidimensional (2D) diffuse gas density in (cm^{-2}) cannot directly be compared with gas density in cm^{-3} units. We therefore converted the observed 2D to 3D geometry, by conservation of the total mass—square area equal to sphere surface—of a 2D circle to a 3D sphere of the diffuse gas that radiates in X-rays. Thus, the area $s_x^2 = 4.\pi\, R_c^2$, where R_c is the cluster effective radii. This equation gives an R_c of $\sim$4.1 pc ($\sim$0.16 deg), so the characteristic plasma volume of the region is $V_x = 4/3\pi R_c^3 = 8.48 \times 10^{57}\ \mathrm{cm}^{-3}$. Using the CWM and the analytic solutions to the density (n_0) in cm^{-3} (see Equation (4) of Cantó et al. 2000), we find $n_0 = 0.06\ \mathrm{cm}^{-3}$, which is the typical mass density contribution from massive stellar winds in the region.

The emission measure of the diffuse X-ray emission is obtained by integration of electron density squared over the emitting volume (EM $= 3/4\pi R_c^3\, n_0^2$); thus, EM $\sim 1.71 \times 10^{55}\ \mathrm{cm}^{-3}$, and XSPEC normalization (Norm $= 10^{-14}\, \mathrm{EM}/(4\,\pi\, D)^2$) of 3.9. With all these parameters, and assuming that the emission is well described by a combination of three thermal plasmas (see Section 6), we simulated a fake X-ray spectrum by assuming APEC models at temperatures $kT \approx$ 0.1, 0.4, and 1.2 keV (see Table 1). In order to compute theoretical absorption-corrected X-ray luminosity, we applied individual multiplicative neutral hydrogen absorption column (using TBabs) to the emission models. Values of $N_{\mathrm{H}} = (0.42,\ 1.1,\ 1.3) \times 10^{22}\ \mathrm{cm}^{-2}$ were obtained from our X-ray spectral fitting results (see Section 6). It should be mentioned that if we adopt the dust column density relationship $N_{\mathrm{H}}/A_v = 1.6 \times 10^{21}\ \mathrm{cm}^{-2}$, which represents the better proxy for the soft X-ray absorption column density from H I maps (Flaccomio et al. 2023), the A_v in the region ranges between 2.6 and 6.8 mag, values that are consistent with the median value of 4.5 mag (Guarcello et al. 2023b). Using these approaches, we predict a theoretical soft X-ray luminosity $L_{\mathrm{X}}^{\mathrm{Soft}} = 2.1 \times 10^{34}$ erg s^{-1} and hard luminosity $L_{\mathrm{X}}^{\mathrm{Hard}} = 0.2 \times 10^{34}$ erg s^{-1}, leading to a total diffuse X-ray luminosity $L_{\mathrm{X}}^{\mathrm{diff}}$ of 2.3×10^{34} erg s^{-1}, for the 0.5–7.0 keV energy band, a factor $\sim$2 lower than spectral fit results. In any case, and for different reasons, diffuse X-ray luminosity computed from spectral fitting or from CWM should be more rigorously considered a lower limit.

Comparing our X-ray flux estimate to that of other SFRs, we find that the diffuse X-ray luminosity in Cygnus OB2 is a factor $\sim$3 larger than that estimated for the Arches cluster (1.6×10^{34} erg s^{-1}; Yusef-Zadeh et al. 2002), $\sim$2 times larger than for the massive NGC 3603 cluster (2.0×10^{34} erg s^{-1}; Moffat et al. 2002), but $\sim$7 times fainter than computed for the Carina Nebula (3.2×10^{35} erg s^{-1}; Townsley et al. 2011a) for the same energy band. These agreements support the idea that the massive stellar content plays a major, but proportional, role in the efficiency of conversion from injected kinetic wind energy through ISM interaction to the diffuse X-ray luminosity, which for Cygnus OB2 is $\sim 3 \times 10^{-4}$.

However, it is plausible that NT processes may be acting efficiently near the massive stars, altering, and perhaps increasing, the diffuse X-ray luminosity of the region. Thus, it is of interest to examine potential NT emission contributions and their implications in a multiwavelength context.

7.2. Nonthermal Contribution to Diffuse X-Ray Emission

Diffuse X-ray emission may also be produced through NT mechanisms. Evidence for NT processes has been uncovered in the Westerlund 1 star cluster by Muno et al. (2006). However, those authors suggested that about 30% of the diffuse X-ray emission continuum would be produced by the unresolved PMS star population in the region, probably through magnetic reconnection flares and/or microflares. The relevant NT emission processes are synchrotron losses (SLs) and IC scattering, which naturally produce more hard ($\geqslant$2 keV) X-rays, and are consequently not trivially distinguishable from the AGN background diffuse contribution. A third process, leading to softer X-rays, is CXE line emission. The relative importance of these mechanisms depends on how, and where, the required population of NT particles are created in the region, the neutral hydrogen density of the local ISM, and also the local magnetic field in the region.

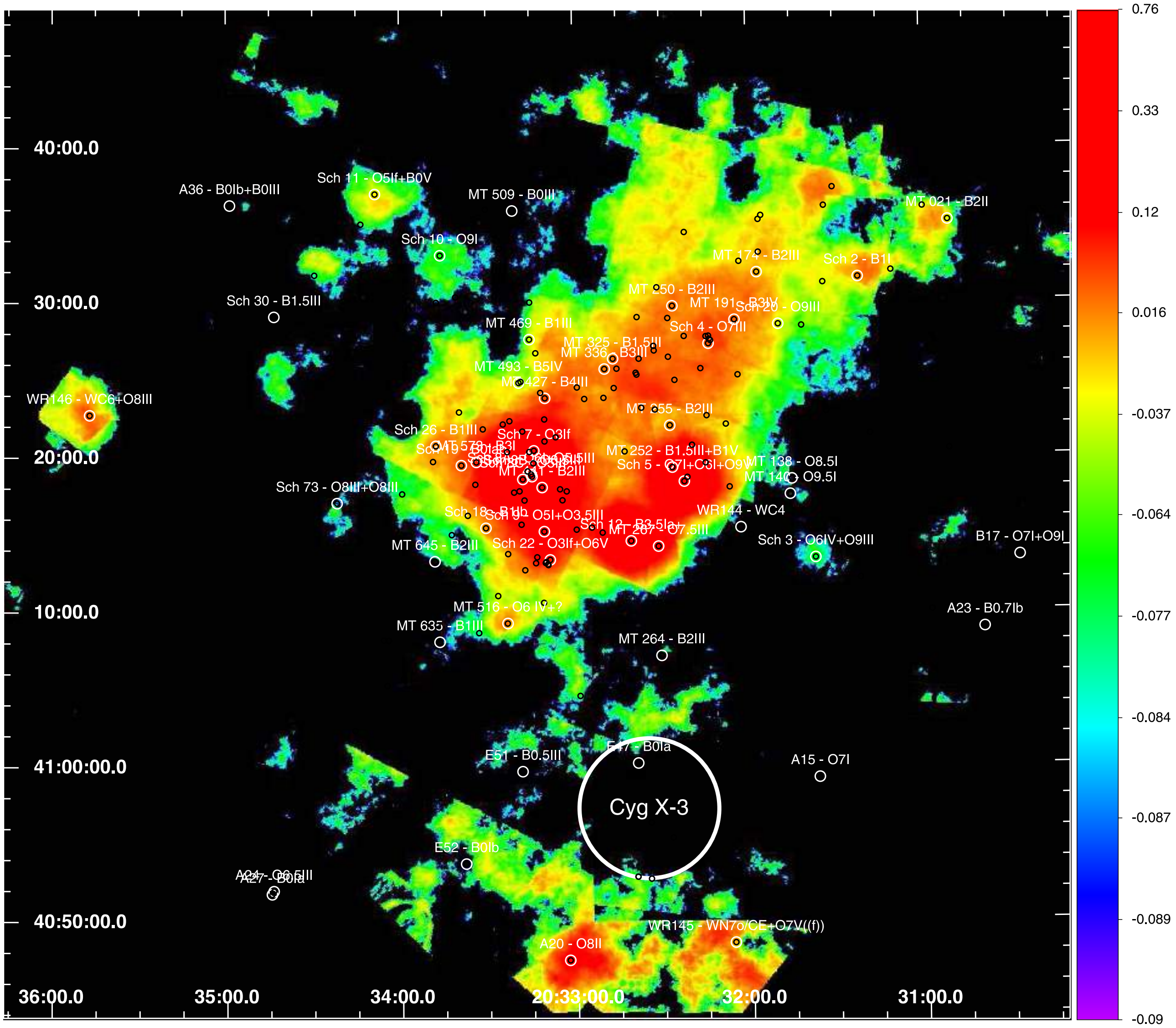

Figure 15. The Cygnus OB2 HR diffuse map in the soft (0.5–2.5 keV) and hard (2.5–7.0 keV) bands. Spatial regions of diffuse gas that correspond to HR values lower than −0.1 were discarded (see Section 4). Small black circles indicate the MS massive stars of the region. Names and labels in white indicate the evolved stars with more intense stellar winds (Wright et al. 2015b). Names are omitted for main-sequence O- and B-type stars that have less massive winds. The X-ray mosaic intensity is logarithmically scaled.

In order to compare relative SL and IC loses, we compute the ratio between the radiation field density ($U_{\rm ph}$) of massive stars of the region and the expected ISM magnetic density ($U_B = B^2/8\pi$) of the region. We adopted a typical ISM magnetic field of $B \sim 4\ \mu$G (Beck 2001) to calculate U_B and used the individual bolometric luminosity (L_7) to compute $U_{\rm ph}$ ($= 5.5 \times 10^{-9}\, L_7 d_{\rm pc}^{-2}$) in erg cm^{-3} around each massive star (Muno et al. 2006). The individual $U_B/U_{\rm ph}$ ratio as a function of distance ($d_{\rm pc}$) for each massive star was calculated, but for simplicity Figure 16 only shows the median and integrated $U_{\rm ph}$ as a function of distance from the stars. The averaged $U_{B=4\mu{\rm G}} \geqslant U_{\rm ph}$ condition is supplied for distances above 0.5 and 1 pc for single MS and evolved massive stars, respectively. We considered the projected density of massive stars in the region, which has a typical value of 0.8 star pc^{-2}, so the respective contributions to $U_{\rm ph}$ from individual massive stars should be added to get a more realistic estimation of the $U_{\rm ph}$. The radiation field hypothetically has a maximum at the center of the diffuse X-ray emission—in agreement with the spatial density of massive stars (centered at R.A. = 20:33:00, decl. = 41:20:00); see Figure 15. Figure 16 shows that SL becomes important only for distances larger than ∼5 pc (∼12.4′) from the center of the region. However, at such a distance, the observed diffuse X-ray emission is absent, or just marginally detected in soft X-rays, so that SLs would not be contributing significantly to the observed X-ray diffuse emission.

Otherwise, IC scattering is a potential loss term for diffuse X-ray emission, feeding off copious UV photons from massive stars. However, the dilution of the UV field ($U_{\rm phot}$) increases with the distance to the stellar source and thus rapidly decreases the energy of the electrons after they leave the vicinity of the shock, imposing a natural "short"-distance restriction for the action of this mechanism. Hence, considering that the luminous (evolved) star shock occurs in the radiative cooling limit, we compared synchrotron to IC losses through the expression $L_{\rm syn}/L_{\rm IC} = U_B/U_{\rm phot} \approx 7.1 \times 10^{-4} B^2/L_6$, where $B = B_{\rm star}(v_{\rm rot}.R/v_\infty)d^{-1}$ and L_6 in $10^6\ L_\odot$ (White & Chen 1995). As $U_{\rm syn}$ and $U_{\rm phot}$ go as the

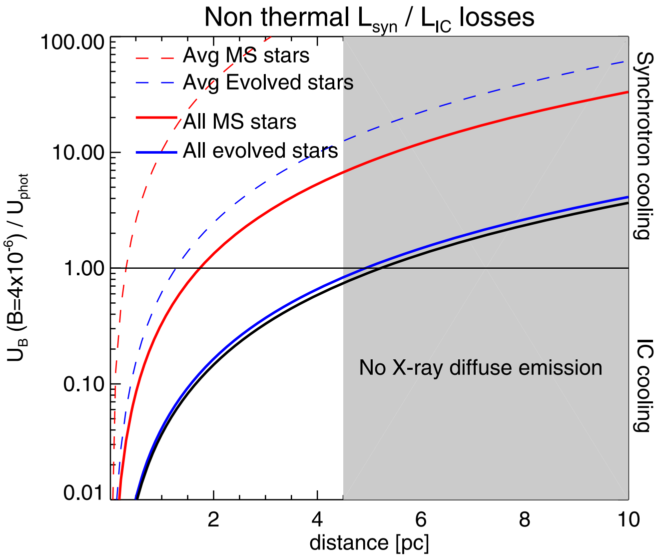

Figure 16. Curves representing the expected relative contribution of synchrotron to IC loses to the diffuse X-ray emission. The black solid line corresponds to the ratio $U_{B=4\mu\mathrm{G}}/U_{\mathrm{ph}}$ accounting for the total contribution from all massive stars of the region with respect to the center of the diffuse emission. The gray region represents distances from the adopted center (R.A. = 20:33:00, decl. = 41:20:00), in which diffuse X-ray emission is not observed.

inverse square of the distance, and adopting typical values for the magnetic fields of the massive stars ($B_{\mathrm{star}} \sim 200$ G), $L_{\mathrm{syn}}/L_{\mathrm{IC}} \approx 10^{-7}$, so the IC process is dominant over SL near the massive stars. However, the energy requirement to raise the input energy of UV photons ($E_{\mathrm{input}} \sim$ 10–20 eV) into the observed X-ray regime of the diffuse emission (E_{out} in 0.5–7.0 keV) requires a population of accelerated electrons of moderate energy (∼5–35 MeV) generated in the inner wind of massive stars, or even from colliding wind regions (Muno et al. 2006). So IC cooling may act in the inner stellar winds and cannot travel far from the acceleration site (Chen 1992; Eichler & Usov 1993); thus, large-scale (few parsecs) IC cooling is not expected to contribute to the observed diffuse X-ray emission.

These theoretical predictions for insignificant contributions from SLs and IC scattering therefore agree with the observed absence of hard (2.5–7.0 keV) diffuse X-ray emission (Figure 14).

Alternatively, there is one further mechanism that could produce NT diffuse X-ray emission. Theoretical (Wise & Sarazin 1989) and, more recently, observational (Townsley et al. 2011a) considerations suggest that highly charged ions associated with hot plasma (from massive stellar winds) could interact with neutral atoms of ambient cool or warm ISM gas via the CXE mechanism. CXE is an NT line-emission mechanism that could produce conspicuous diffuse X-ray emission at soft (line-emission) energies, even when such interactions occur on spatial scales of several tenths of parsecs (Montmerle & Townsley 2012). Calculations from Wise & Sarazin (1989) have shown that CXE emission is negligible in the case of supernova remnants with fast shocks but becomes important for less energetic cases, such as hot gas interacting with cold, dense ISM structures. The process is more efficient for lighter elements (Lallement 2004), and a wide variety of emission lines below 2 keV are expected from elements in various ionization states, with no continuum contribution. In Carina, for example, lines and possible elements responsible for them are 0.64 keV (O), 0.77 keV (O or Fe), 1.07 keV (Ne), 1.34 + 1.54 keV (Mg), 1.80 keV (Si), and some faint lines at harder X-ray energies such as 2.61 keV (S) and 6.50 keV (Fe) (Townsley et al. 2011a). Such emission has also been suggested in other massive SFRs for which the data were of sufficient quality (Townsley et al. 2011b). In Figure 17 we inspected the neighborhood of Cygnus OB2 in a multiwavelength approach, by searching for plausible regions for CXE emission, where soft X-ray diffuse emission coexists with "warm" (≈100–150 K) and cold (≈10–50 K) gas structures observed in the infrared (Spitzer and Hershel data, respectively). Just four zones satisfy this condition, one to the north and the others toward the center of the region. However, soft diffuse emission luminosity in these three regions is low enough to search for narrowband images at excesses produced by CXE emission-line energies, e.g., ∼0.6–0.8 keV for O and/or Fe lines, and ∼1.0–1.6 keV for Ne and/or Mg. Although the poor photon statistics in the X-ray spectra of these regions do not allow us to confirm the presence of line emission from He-like and H-like states of the elements C, N, and O, the mere existence of soft diffuse X-ray emission, even far from the massive stars, would be considered a favorable place for the CXE mechanism occurring in Cygnus OB2.

The multiwavelength image of the region (see Figure 17) also shows that most X-ray diffuse emission is spatially coincident with regions of low infrared surface brightness, which is coincident with regions of low ISM extinction. This suggests that the X-ray plasma is volume filling, rather than edge brightened, just as was found for the Carina Nebula (Townsley et al. 2011a) and other giant H II regions (Townsley et al. 2011b). This is an indirect observational probe that in the case of Cygnus OB2 powerful stellar winds from massive stars primarily collide between the OB winds rather than independently with the exterior cold cloud, which is in concordance with the Cantó et al. (2000) 3D modeling of SFRs with a high-density population of massive stars.

Finally, and for the first time, we have resolved X-ray diffuse emission halos at subparsec scales around some evolved massive stars of the region (see figures and respective comments in the Appendix). We defer a more detailed study of this phenomenon to future work.

8. Summary

A thorough and detailed analysis of 40 Chandra ACIS-I observations of the Cygnus OB2 association, including the removal of the 7924 X-ray pointlike sources detected, has revealed the diffuse X-ray emission that permeates the region. We have mapped a region ∼30 pc^2 across at a spatial resolution reaching down to a few thousand astronomical units. The main findings of the study of this diffuse emission are as follows:

1. Large-scale X-ray diffuse emission was seen in the broad 0.5–7.0 keV energy band and was also detected in the soft (0.5–1.2 keV) and medium (1.2–2.5 keV) bands. A marginal detection of diffuse emission was made in the hard (2.5–7.0 keV) band.
2. The total diffuse X-ray emission luminosity was found to be $L_X^{\mathrm{diff}} \approx 4.2 \times 10^{34}$ erg s^{-1} (0.5–7.0 keV) and was well represented by a three-component thermal plasma model with typical temperatures of $kT \approx$ 0.11, 0.40, and 1.18 keV (1.2, 4.9, and 14 MK, respectively).

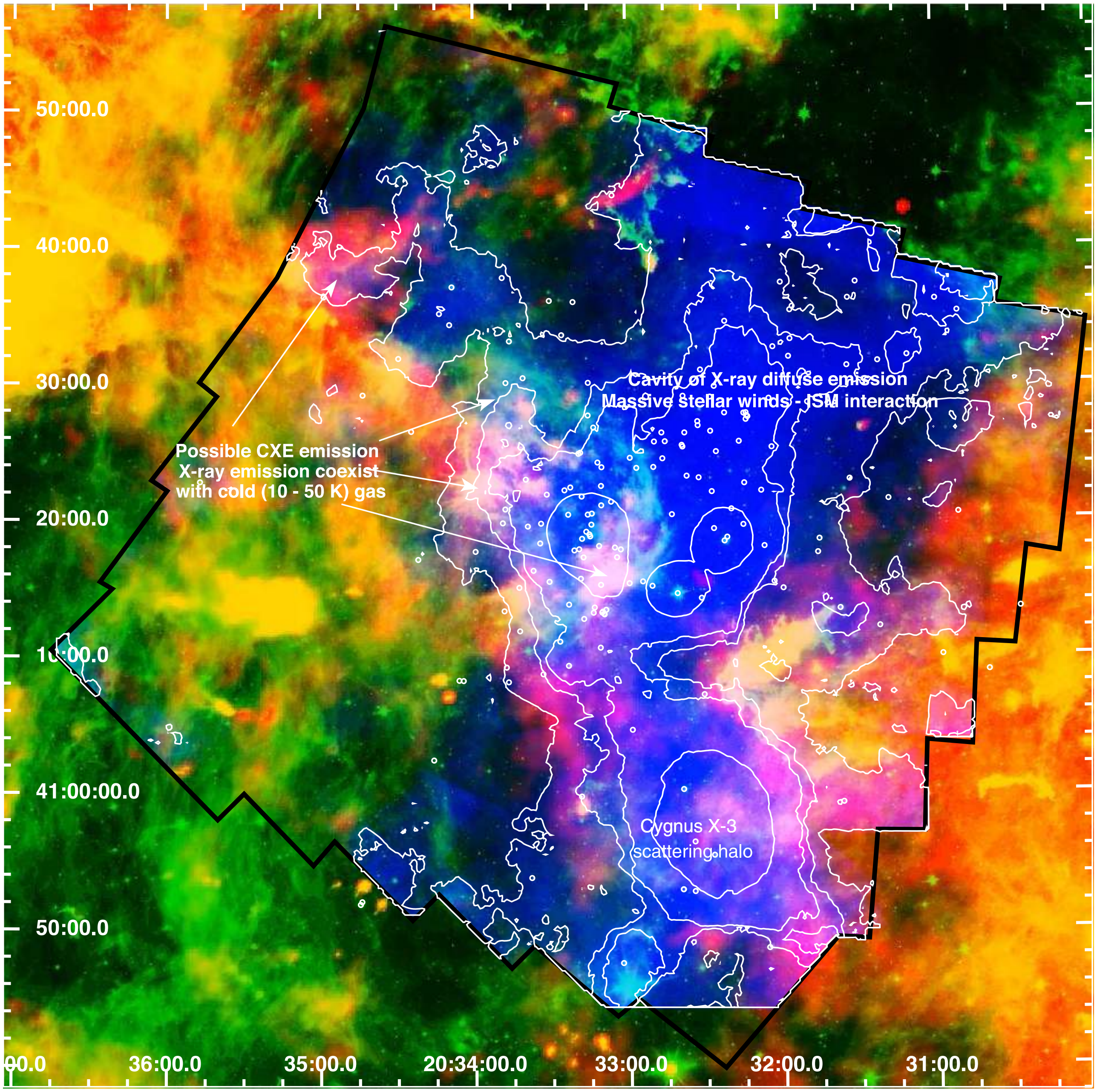

Figure 17. The neighborhood of Cygnus OB2. The ACIS-I mosaic of the Cygnus OB2 survey is outlined in black. Small circles indicate the massive OB star content of the region, regardless of spectral type and evolutionary class (Wright et al. 2015b). Diffuse X-ray contours corresponding to flux levels of (3.0, 3.7, 4.1, 4.7, 8.3) $\times$ 10^{-10} photons cm^{-2} s^{-1} $arcsec^{-2}$ are shown in white. The false RGB color image was composed as follows: the Herschel 500 μm ($T \approx 10$ K) cold gas emission in red, the 8 μm Spitzer IRAC image for the warm gas ($T \approx 150$ K) in green, and the diffuse X-ray emission in the 0.5–2.5 keV energy range in blue. There are also four arrows that indicate the regions that show signs of the coexistence of 10 K cold ISM gas and hot diffuse X-rays, which are likely scenarios for CXE emission.

3. The extended moderate energy emission likely arises from O-type star winds thermalized by wind−wind collisions in the most populated regions of the association, while the supersoft (SS) emission probably arises from less energetic termination shocks against the surrounding ISM. The SS diffuse emission appears more dispersed than that at soft and medium energies, indicating diffusive motions of hot gas on 2–3 pc scales.
4. The H I absorption column density was constrained with three individual N_H models, which on stacked spectra are $N_H = (0.42, 1.12, 1.30) \times 10^{22}$ cm^{-2}. At the center of the region, where most of the massive stars are located, N_H seems to be slightly lower than found for outer regions. The diffuse X-ray emission is then spatially coincident with low-extinction regions (and low ISM densities), which we attribute to powerful stellar winds from massive stars and their interaction with the local ISM. It is volume filling, rather than edge brightened, as has been found for other SFRs.
5. An assessment of potential NT diffuse emission sources finds that both synchrotron and IC scattering are not likely to contribute significantly to the observed large-scale diffuse emission. A full assessment of a possible CXE emission signal is challenging owing to the large

extinction that renders soft X-ray emission difficult to observe. By the way, this would require a more detailed spectral analysis.

6. Examination of the diffuse emission maps on smaller scales reveals X-ray halos around evolved massive stars. This is the first time such emission structures have been detected.

The results presented here highlight the value of large-scale X-ray surveys for understanding the energetics and feedback in massive SFRs, in addition to assessing their otherwise hidden or inconspicuous stellar content.

Acknowledgments

We thank the referee Dr. David Helfand for many corrections to and very helpful suggestions for our article. J. F.A.-C. is a researcher of CONICET and acknowledges their support. The research leading to these results has received funding from the European Union's Horizon 2020 Programme under the AHEAD project (grant agreement No. 654215). J.J. D. and V.K. were supported by NASA contract NAS8-03060 to the Chandra X-ray Center (CXC) and thank the director, B. Wilkes, and the science team for continuing support and advice. M.G.G. and N.J.W. were supported by Chandra grant GO0-11040X during the course of this work. M.G.G. also acknowledges the grant PRIN-INAF 2012 (P.I. E. Flaccomio). N.J.W. acknowledges a Royal Astronomical Society research fellowship and an STFC Ernest Rutherford Fellowship (grant No. ST/M005569/1). N.S. acknowledges support by the French ANR and the German DFG through the project "GENESIS" (ANR-16-CE92-0035-01/DFG1591/2-1). We kindly thank Dr. Patrick Broos of the Penn State University's astrophysics group, who shared some private AE scripts for the diffuse X-ray analysis of the Chandra ACIS-I observations. This research made use of Montage, funded by the National Aeronautics and Space Administration's Earth Science Technology Office, Computation Technologies Project, under Cooperative Agreement No. NCC5-626 between NASA and the California Institute of Technology. Montage is maintained by the NASA/IPAC Infrared Science Archive.

Appendix

Diffuse X-Ray Emission of Individual ObsID Maps

In Figures 18–21, we show the individual diffuse X-ray maps (flux and HR) for the entire set of observations performed for the Cygnus OB2 Chandra ACIS-I survey. Each map is 17 arcmin^2. The first and third columns show flux in the 0.5–7.0 keV energy band. Using the thermal model of the X-ray spectral fit (see Section 6), we have computed the validated photon keV-to-erg conversion in the 0.5–7.0 keV band to be 1 photon $= 4.18 \times 10^{-9}$ erg, which allows for conversion of diffuse maps of observed photon counts to absorbed flux. The X-ray flux is in CGS photon units. HR images are displayed in the second and fourth columns, respectively. They were computed as the ratio (S – H)/(S + H). True diffuse emission was only considered whenever $\mathrm{HR} > -0.1$, corresponding to the colors green, yellow, and red in the HR maps (see Section 4 for details). Intensities are illustrated on a single color scale of $\log(L_{\mathrm{X}}) = [-17.08, -16.63]$ and $\mathrm{HR} = [-0.3, 0.5]$ to facilitate comparison between flux and HR maps, respectively. The filled and open symbols all over the maps refer to massive stars with and without intrinsic X-ray emission, respectively. Stars correspond to evolved objects, while circles represent MS stars. Crosses represent massive OB-type stellar candidates from Wright et al. (2015c).

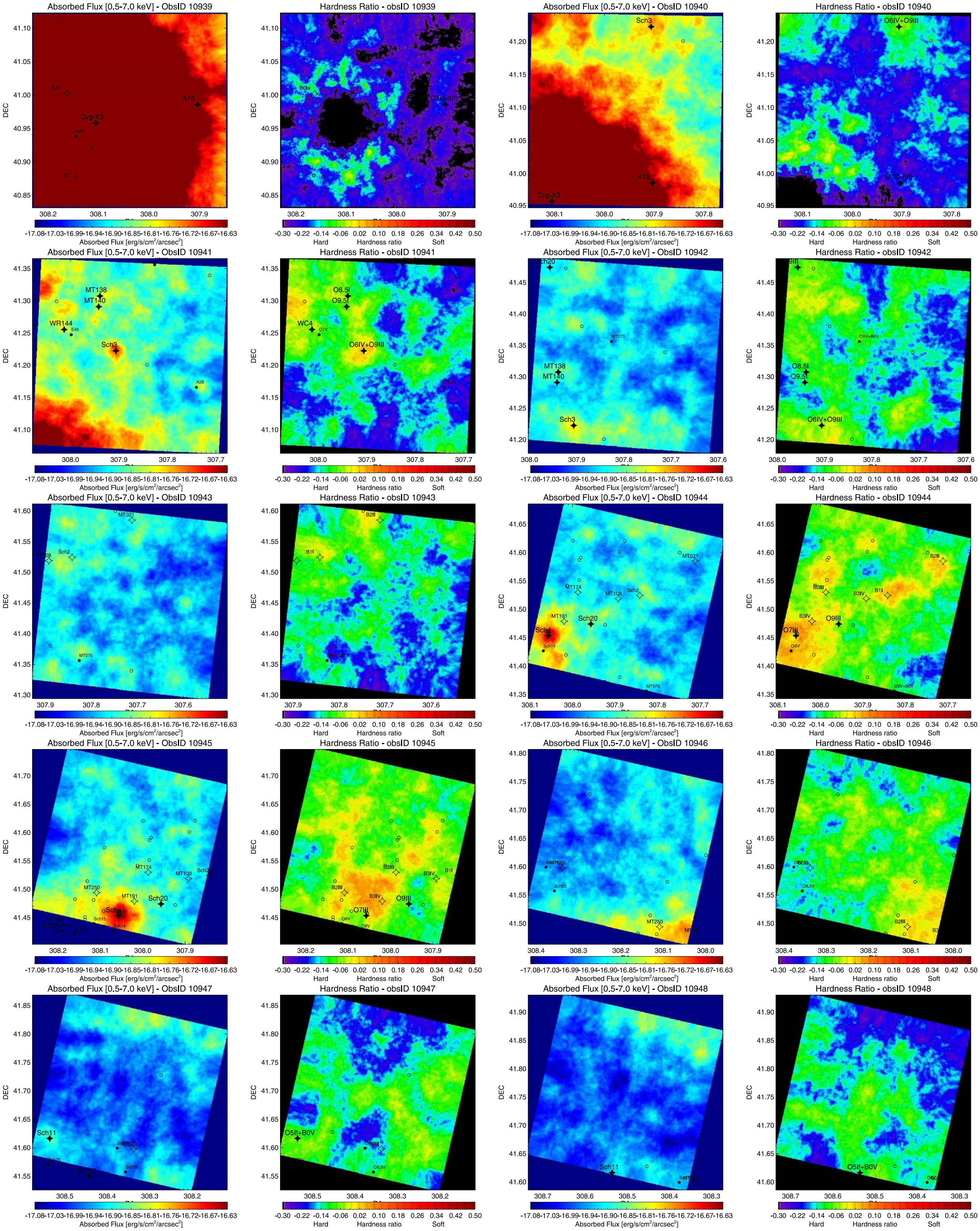

Figure 18. *Diffuse X-ray emission maps for ObsIDs 10939 to 10941:* These observations are affected by the X-ray dust scattering halo produced by X-ray photons from the background source Cygnus X-3. The massive evolved binary system (O6IV + O9III) Schulte #3 shows a diffuse X-ray halo, with a typical HR ∼ 0.05–0.16. The single evolved stars WR 144, MT 138, and MT 140 do not show halo-like emission but appear to contribute to diffuse structures in the nearby regions through wind–ISM interactions (see discussion in Section 7). *Maps for ObsIDs 10942 to 10944:* Schulte #4 (O7III + ?) has an associated diffuse X-ray halo, even though it is a relatively faint X-ray point source (net counts 296 photons). In contrast, Schulte #20 (O9 III) does not produce a diffuse halo, although faint diffuse structures appear to be present (see HR maps), similar to the cases of the other evolved B-type massive stars (MT 191, 174, 108 and Schulte #2). *Maps for ObsIDs 10945 to 10948:* The diffuse contribution in the lower right corner of ObsID 10947 is the Cygnus X-3 X-ray binary dust scattering halo (see discussion in Section 4.2).

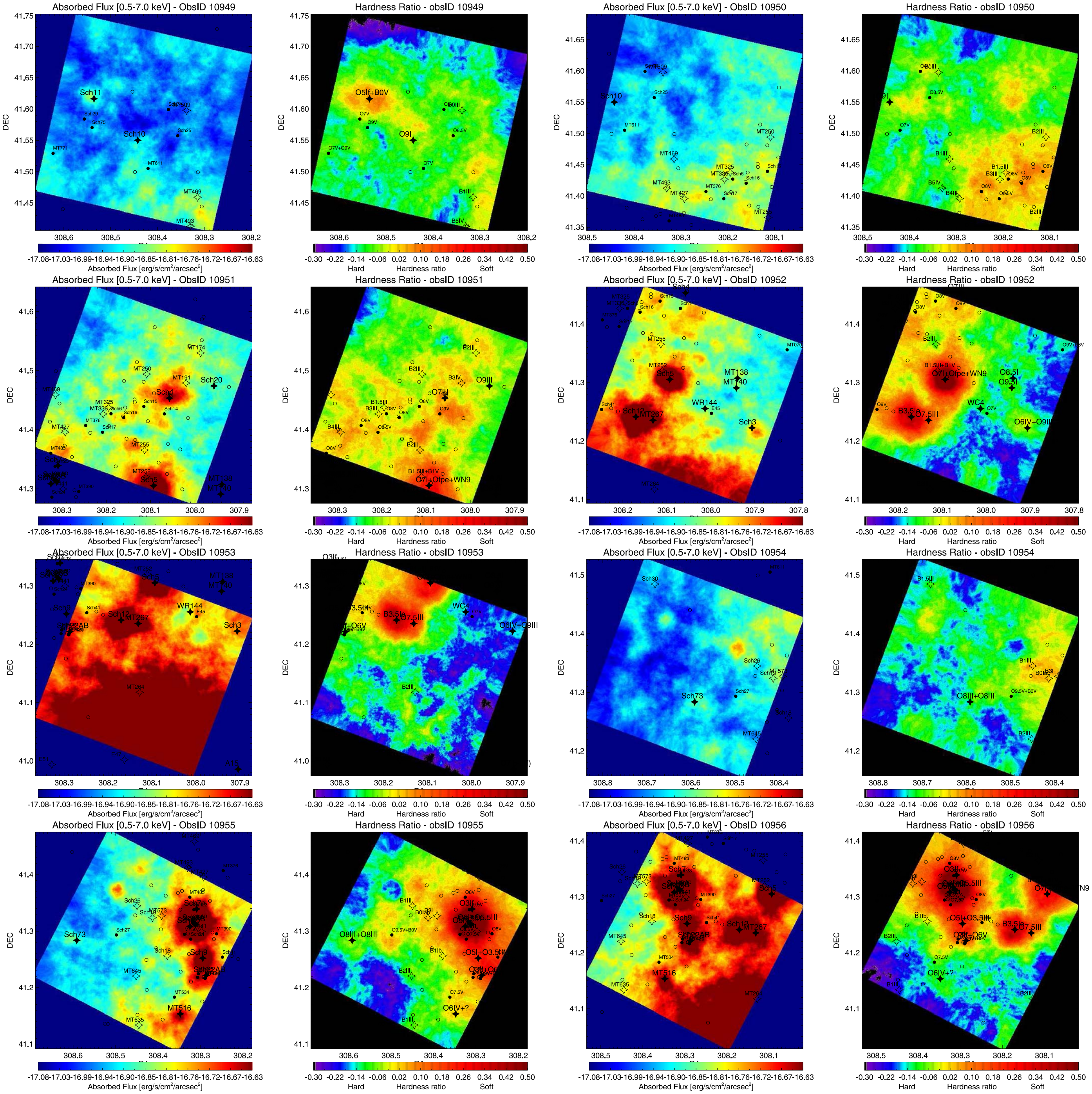

Figure 19. *Diffuse X-ray emission maps for ObsIDs 10949 to 10950:* The evolved massive binary system (O5If + B0V) Schutle #11 has a diffuse X-ray halo, while the evolved massive (O9I) Schutle #10 does not. In ObsID 10950, a large diffuse X-ray structure follows the spatial distribution of massive stars, even though all these stars do not have detectable intrinsic X-ray emission. This indicates that the diffuse X-ray emission is independent of any intrinsic X-ray emission of the massive stars, but not from their stellar wind properties. *Maps for ObsIDs 10951 to 10953:* The very massive evolved binary stars, Schutle #5 and #12, show clear X-ray halos. In ObsID 10953, a large diffuse structure is produced by the Cygnus X-3 X-ray binary dust scattering halo (see discussion in Section 4.2). *Maps for ObsIDs 10954 to 10956:* In the upper and middle maps, to the NW of Schutle #26, at R.A. = 308.48 and decl. = 41.375, there is an intriguing diffuse X-ray emission structure that does not correlate with any known massive star of the region. More interestingly, it has quite a hard spectrum (HR $\leqslant -0.15$). The rest of the diffuse soft X-ray emission is clearly related to the massive stellar content of the region, especially the evolved stars. Note that MT 516 (O6IV + ?) produces harder diffuse emission than is typical of the other evolved massive stars. Colliding winds and diffusive motion of hot gas could be a plausible explanation for it.

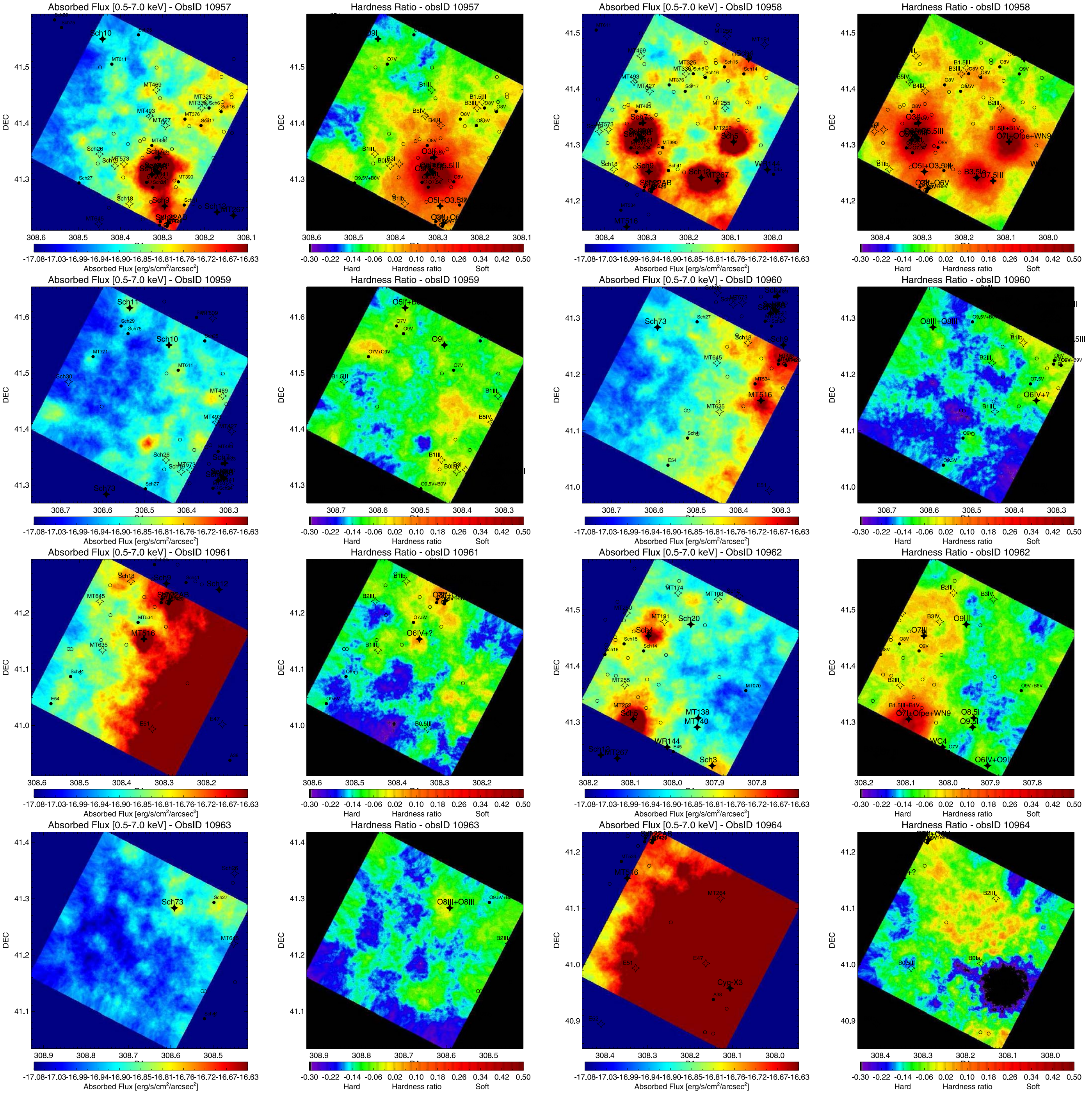

Figure 20. *Diffuse X-ray emission maps for ObsID 10957 to 10959:* Soft X-ray emission is dominated by massive stars, with halos around some of the evolved ones, while more diffuse hot gas follows the spatial distribution of late O and/or early B MS stars. Again, the intriguing diffuse X-ray emission structure at R.A. = 308.48 and decl. = 41.375 appears with a clear spherical distribution of hard diffuse emission. *Maps for ObsIDs 10960 to 10962:* Note that a large part of ObsID 10961 is affected by scattering from Cyg X-3. The maps show clear evidence of X-ray halos around the massive evolved stars MT 516 (O6IV), Schutle #4 (O7III), and Schutle #5 (O7I + Ofpe + WN9). Diffuse X-ray emission maps for ObsID 10963 to 10964. The intrinsically X-ray-faint Schutle #73 (O8III + O8III) binary exhibits a diffuse X-ray halo, while the binary Schutle #11 (O5If + B0V) shows marginal evidence for a halo in the HR map. Of all the massive stars in the MS phase, the massive binary MT 771 (O7V + O9V) is the only one that has an associated diffuse X-ray halo. Another intriguing diffuse hard X-ray emission structure at R. A. = 308.765 and decl. = 41.585 appears to the south of A36. A more detailed examination of these intriguing results will be presented in future work.

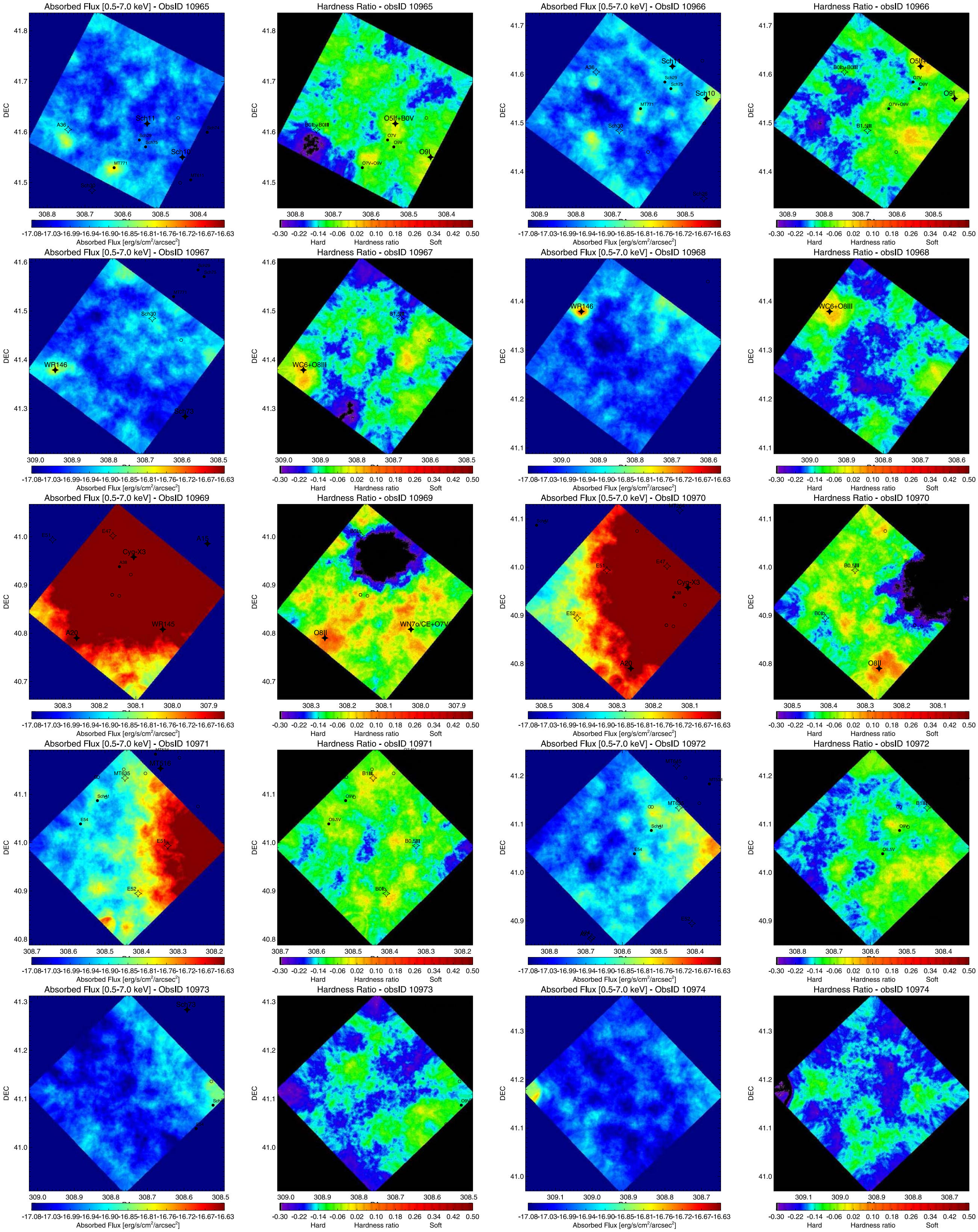

Figure 21. *Maps for ObsIDs 10965 to 10968:* The most conspicuous diffuse halo appears to be related to the strong wind–ISM interaction of WR 146. The structure spans a radial distance of more than 0.3 pc. *Diffuse X-ray emission maps for ObsIDs 10969 to 10971:* Here, the background radiation from Cygnus X-3 leads to scattering of X-ray photons over a large spatial scale, with an extension of about 3 pc (∼8′; see discussion in Section 4.2). The suspected pre-supergiant single star A20 (O8II) has an associated X-ray halo, although this is partially masked by the Cyg X-3 scattered background. *Maps for ObsIDs 10972 to 10974:* The left corner of ObsID 10974 shows a very intriguing partial view of an intense diffuse X-ray halo, which is also hard, contrary to what we observed around massive stars. Note in the flux and HR maps the existence of faint diffuse hard X-ray emission with a faint "jet-like" asymmetry.

ORCID iDs

J. F. Albacete-Colombo https://orcid.org/0000-0001-8398-0515
J. J. Drake https://orcid.org/0000-0002-0210-2276
E. Flaccomio https://orcid.org/0000-0002-3638-5788
V. Kashyap https://orcid.org/0000-0002-3869-7996
M. G. Guarcello https://orcid.org/0000-0002-3010-2310
G. Micela https://orcid.org/0000-0002-9900-4751
M. McCollough https://orcid.org/0000-0002-8384-3374
N. Schneider https://orcid.org/0000-0001-6720-5519

References

Albacete Colombo, J. F., Flaccomio, E., Micela, G., Sciortino, S., & Damiani, F. 2007, A&A, 464, 211
Albacete-Colombo, J. F., Flaccomio, E., Drake, J. J., et al. 2023, ApJS, 269, 11
Arnaud, K. A. 1996, ASP Conf. Ser. 101, Astronomical Data Analysis Software and Systems V, ed. G. H. Jacoby & J. Barnes, (San Francisco, CA: ASP), 17
Beck, R. 2001, SSRv, 99, 243
Broos, P., Townsley, L., Getman, K., & Bauer, F., 2012 AE: ACIS Extract, Astrophysics Source Code Library, ascl:1203.001
Bruhweiler, F. C., Freire Ferrero, R., Bourdin, M. O., & Gull, T. R. 2010, ApJ, 719, 1872
Butt, Y. M., Drake, J., Benaglia, P., et al. 2006, ApJ, 643, 238
Cantó, J., Raga, A. C., & Rodríguez, L. F. 2000, ApJ, 536, 896
Cash, W., Charles, P., Bowyer, S., et al. 1980, ApJL, 238, L71
Chen, W. 1992, PhD thesis, Johns Hopkins Univ. Baltimore
Comerón, F., Pasquali, A., Rodighiero, G., et al. 2002, A&A, 389, 874
Corral, A., Della Ceca, R., Caccianiga, A., et al. 2011, A&A, 530, A42
Diehl, S., & Statler, T. S. 2006, MNRAS, 368, 497
Dorland, H., & Montmerle, T. 1987, A&A, 177, 243
Drew, J. E., Greimel, R., Irwin, M. J., & Sale, S. E. 2008, MNRAS, 386, 1761
Dwarkadas, V. V., & Rosenberg, D. L. 2013, HEDP, 9, 226
Eichler, D., & Usov, V. 1993, ApJ, 402, 271
Feigelson, E. D., Getman, K., Townsley, L., et al. 2005, ApJS, 160, 379
Flaccomio, E., Albacete-Colombo, J. F., Drake, J. J., et al. 2023, ApJS, 269, 12
Fruscione, A. 2014, ChNew, 21, 24
Getman, K. V., Broos, P. S., Feigelson, E. D., et al. 2011, ApJS, 194, 3
Getman, K. V., Feigelson, E. D., Grosso, N., et al. 2005, yCat, J/ApJS/160/353
Guarcello, M. G., Drake, J. J., Wright, N. J., et al. 2023a, ApJS, 269, 9
Guarcello, M. G., Drake, J. J., Wright, N. J., et al. 2023b, ApJS, 269, 13
Güdel, M., Briggs, K. R., Montmerle, T., et al. 2008, Sci, 319, 309
Hanson, M. M. 2003, ApJ, 597, 957
Hickox, R. C., & Markevitch, M. 2006, ApJ, 645, 95
Kashyap, V. L., Guarcello, M. G., Wright, N. J., et al. 2023, ApJS, 26, 10
Koljonen, K. I. I., Hannikainen, D. C., McCollough, M. L., Pooley, G. G., & Trushkin, S. A. 2010, MNRAS, 406, 307
Lallement, R. 2004, A&A, 422, 391
Lamers, H. J. G. L. M., Snow, T. P., & Lindholm, D. M. 1995, ApJ, 455, 269
Massey, P., & Thompson, A. B. 1991, AJ, 101, 1408
May, B., & Keel, W. C. 2008, AAS Meeting, 211, 157
McCollough, M. L., Corrales, L., & Dunham, M. M. 2016, ApJL, 830, L36
McCollough, M. L., Smith, R. K., & Valencic, L. A. 2013, ApJ, 762, 2
Moffat, A. F. J., Corcoran, M. F., Stevens, I. R., et al. 2002, ApJ, 573, 191
Montmerle, T., & Townsley, L. K. 2012, AN, 333, 355
Muno, M. P., Law, C., Clark, J. S., et al. 2006, ApJ, 650, 203
Nazé, Y., Chu, Y.-H., Guerrero, M. A., et al. 2002, AJ, 124, 3325
Pauldrach, A., Puls, J., & Kudritzki, R. P. 1986, A&A, 164, 86
Pittard, J. M., & Parkin, E. R. 2010, MNRAS, 403, 1657
Polcaro, V. F., Giovannelli, F., Manchanda, R. K., Norci, L., & Rossi, C. 1991, A&A, 252, 590
Preibisch, T., McCaughrean, M. J., Grosso, N., et al. 2005, ApJS, 160, 582
Rauw, G., Nazé, Y., Wright, N. J., et al. 2015, ApJS, 221, 1
Reipurth, B., & Schneider, N. 2008, in Handbook of Star Forming Regions, Volume I: The Northern Sky, ed. B. Reipurth (San Francsico, CA: ASP), 36
Schneider, N., Bontemps, S., Simon, R., et al. 2006, A&A, 458, 855
Schulte, D. H. 1956, ApJ, 124, 530
Smith, R. K., Brickhouse, N. S., Liedahl, D. A., & Raymond, J. C. 2001, ApJL, 556, L91
Smith, R. K., & Hughes, J. P. 2010, ApJ, 718, 583
Stevens, I. R., & Hartwell, J. M. 2003, MNRAS, 339, 280
Strickland, D. K., & Stevens, I. R. 1998, MNRAS, 297, 747
Townsley, L. K., Broos, P. S., Chu, Y.-H., et al. 2003, RMxAC, 15, 190
Townsley, L. K., Broos, P. S., Chu, Y.-H., et al. 2011a, ApJS, 194, 15
Townsley, L. K., Broos, P. S., Chu, Y.-H., et al. 2011b, ApJS, 194, 16
Uyaniker, B., Fürst, E., Reich, W., Aschenbach, B., & Wielebinski, R. 2001, A&A, 371, 675
Vink, J. S., de Koter, A., & Lamers, H. J. G. L. M. 2001, A&A, 369, 574
Vink, J. S., Drew, J. E., Steeghs, D., et al. 2008, MNRAS, 387, 308
Weaver, R., McCray, R., Castor, J., Shapiro, P., & Moore, R. 1977, ApJ, 218, 377
White, R. L., & Chen, W. 1995, in IAU Symp. 163, Wolf-Rayet Stars: Binaries; Colliding Winds; Evolution, ed. K. A. van der Hucht & P. M. Williams (Dordrecht: Kluwer), 438
Wilms, J., Allen, A., & McCray, R. 2000, ApJ, 542, 914
Wise, M. W., & Sarazin, C. L. 1989, ApJ, 345, 384
Wright, N. J., & Drake, J. J. 2009, ApJS, 184, 84
Wright, N. J., Drake, J. J., Drew, J. E., et al. 2012, ApJL, 746, L21
Wright, N. J., Drake, J. J., Guarcello, M. G., et al. 2023a, ApJS, 269, 7
Wright, N. J., Drake, J. J., Guarcello, M. G., Kashyap, V. L., & Zezas, A. 2023b, ApJS, 269, 8
Wright, N. J., Drew, J. E., & Mohr-Smith, M. 2015b, MNRAS, 449, 741
Wright, N. J., Drew, J. E., & Mohr-Smith, M. 2015c, yCat, 744, 90741
Wright, N. J., Parker, R. J., Goodwin, S. P., & Drake, J. J. 2014b, MNRAS, 438, 639
Yusef-Zadeh, F., Law, C., Wardle, M., et al. 2002, ApJ, 570, 665